J. Fluid Mech. (2025), *vol.* 1007, A3, doi:10.1017/jfm.2025.139

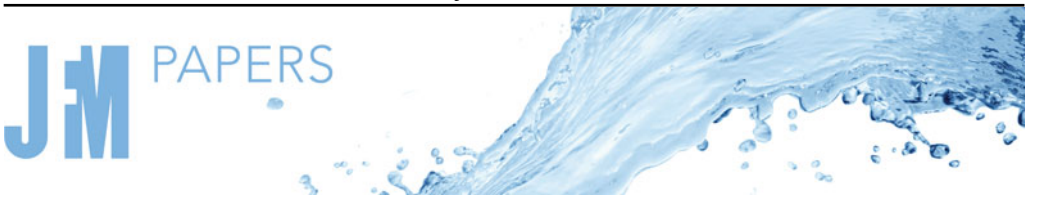

Small-scale dynamics and structure of free-surface turbulence

Yinghe Qi[1], **Yaxing Li**[2] **and Filippo Coletti**[1]

[1]Department of Mechanical and Process Engineering, ETH Zurich, 8092 Zurich, Switzerland

[2]Department of Engineering Mechanics, School of Aeronautics and Astronautics, Zhejiang University, Hangzhou, PR China

Corresponding authors: Yinghe Qi, yingqi@ethz.ch; Yaxing Li, yaxingli@zju.edu.cn

(Received 23 August 2024; revised 26 January 2025; accepted 28 January 2025)

The dynamics of small-scale structures in free-surface turbulence is crucial to large-scale phenomena in natural and industrial environments. Here, we conduct experiments on the quasi-flat free surface of a zero-mean-flow turbulent water tank over the Reynolds number range $Re_\lambda = 207$–312. By seeding microscopic floating particles at high concentrations, the fine scales of the flow and the velocity-gradient tensor are resolved. A kinematic relation is derived expressing the contribution of surface divergence and vorticity to the dissipation rate. The probability density functions of divergence, vorticity and strain rate collapse once normalised by the Kolmogorov scales. Their magnitude displays strong intermittency and follows chi-square distributions with power-law tails at small values. The topology of high-intensity events and two-point statistics indicate that the surface divergence is characterised by dissipative spatial and temporal scales, while the high-vorticity and high-strain-rate regions are larger, long-lived, concurrent and elongated. The second-order velocity structure functions obey the classic Kolmogorov scaling in the inertial range when the dissipation rate on the surface is considered, with a different numerical constant than in three-dimensional turbulence. The cross-correlation among divergence, vorticity and strain rate indicates that the surface-attached vortices are strengthened during downwellings and diffuse when those dissipate. Sources (sinks) in the surface velocity fields are associated with strong (weak) surface-parallel stretching and compression along perpendicular directions. The floating particles cluster over spatial and temporal scales larger than those of the sinks. These results demonstrate that, compared with three-dimensional turbulence, in free-surface turbulence the energetic scales leave a stronger imprint on the small-scale quantities.

Key words: waves/free-surface flows

1. Introduction

From a cup of stirred coffee to the flow in rivers, lakes and oceans, free-surface turbulence is ubiquitous in various natural and industrial environments. The dynamics of the free surface affects the exchange of mass, momentum and energy with the bulk, and thus plays an essential role at the global scale including the exchange of gas between the atmosphere and ocean (Jähne & Haußecker 1998; Veron 2015), the transport of oceanic pollutants such as microplastics (Zhang 2017; Mountford & Morales Maqueda 2019; van Emmerik & Schwarz 2020) and the blooming of phytoplankton (Durham *et al.* 2013; Lindemann *et al.* 2017). When the surface is significantly deformed or broken, strong energy exchanges take place between the turbulence in the bulk and the free surface (Brocchini & Peregrine 2001; Deike 2022). Even when the deformation of the latter is negligibly small, however, the dynamics is highly complex (Magnaudet 2003). Here, we focus on such a regime, considering the fundamental case in which the turbulence below the quasi-flat free surface is approximately homogeneous and isotropic. In particular, we focus on the fine-scale structure, topological properties and the dynamics of the surface flow.

The study of free-surface turbulence can be traced back to Uzkan & Reynolds (1967) and Thomas & Hancock (1977) who investigated grid turbulence adjacent to a solid wall moving at the same velocity as the mean flow. Those experimental studies showed that the surface-normal velocity fluctuations decay to vanishingly small levels over a near-wall region (later termed the source layer) whose thickness is roughly one integral length scale. Following these works, Hunt & Graham (1978) proposed a theoretical framework based on rapid distortion theory (RDT), describing the inviscid response of homogeneous and isotropic turbulence (HIT) to the insertion of an impermeable surface. They identified two layers: the source layer, and a viscous layer where the shear stress along the wall is brought to zero. Their predictions compared favourably with free-surface turbulence experiments in stirred tanks (Brumley & Jirka 1987; Variano & Cowen 2013) as well as direct numerical simulations (Walker *et al.* 1996; Shen *et al.* 1999; Guo & Shen 2010; Herlina & Wissink 2014) and large eddy simulations (Calmet & Magnaudet 2003). Perot & Moin (1995) gave a different interpretation of the interaction between the turbulence in the bulk and the non-deformable free surface, proposing that the imbalance between upwellings and downwellings (carrying fluid to and from the surface, respectively) determines the net intercomponent energy transfer. The issue was further examined by Magnaudet (2003) who found that RDT is a correct leading-order approximation of the shear-free boundary layer in the limit of large Reynolds number. The latter is typically defined as $Re_T = 2u'\mathcal{L}/\nu$, where u', $\mathcal{L}$ and ν are the root mean square (r.m.s.) velocity fluctuation, the integral scale of the turbulence in the bulk and the kinematic viscosity, respectively. The validity of the Hunt & Graham (1978) theory for single-point statistics and sufficiently high Re_T was recently confirmed experimentally by Ruth & Coletti (2024).

The majority of the aforementioned studies focused on the evolution of the turbulence below the free surface, while less is known regarding the dynamics on the flow along the surface itself. Its topology has been explored mostly in open channel flows, both experimentally (Komori *et al.* 1989; Kumar *et al.* 1998; Nikora *et al.* 2007; Tamburrino & Gulliver 2007) and numerically (Pan & Banerjee 1995; Nagaosa 1999; Lovecchio *et al.* 2013, 2015). Those studies emphasised the link between the structures generated in the near-wall boundary layer and those observed along the surface. These showed similarity to two-dimensional (2-D) turbulence, particularly the persistence of surface-attached vortices, as well as some evidence of an inverse energy cascade.

The flow along the surface above HIT was considered in a series of seminal papers (Eckhardt & Schumacher 2001; Goldburg *et al.* 2001; Boffetta *et al.* 2004; Cressman

et al. 2004; Larkin *et al.* 2009). The authors explored features including the velocity structure functions, which were found to scale approximately as in three-dimensional (3-D) turbulence, and the velocity gradients, which were highly intermittent. Moreover, they highlighted the compressible nature of the surface velocity field, leading to dense long-lived clusters of floating particles. Comparisons between computer simulations and laboratory observations were hampered by challenges associated with the free-surface boundary condition. In the simulations, the free surface was treated as a rigid lid, which Shen *et al.* (1999) demonstrated could cause significant misestimation of the pressurestrain correlation even in the limit of small deformations. In the experiments, the floating particles used to image the surface flow tended to create a layer of agglomerated particles (Cressman *et al.* 2004; Turney & Banerjee 2013).

Simulations capturing the liquid interface above forced turbulent flows were conducted by Shen *et al.* (1999) and Guo & Shen (2010), including regimes of low Froude number, i.e. in which the surface tension allows only small deformations. They stressed the dynamic importance of upwelling motions in connecting vortices to the free surface. There, upwellings create hairpin structures whose head dissipates rapidly in the viscous layer with the two legs connecting perpendicularly to the free surface. This suggested that upwellings lead to the increase of the number of surface-attached vortices, as later confirmed by the simulations by Babiker *et al.* (2023). These authors found a strong correlation between the number of surface-attached vortices and the surface velocity divergence, which in turn is related to the presence of upwellings/downwellings (see Guo & Shen (2010); Ruth & Coletti (2024)). Herlina & Wissink (2014, 2019) used interface-resolving simulations to investigate the gas transfer across the surface above HIT for a range of Re_T. They found that the increase of fine-scale structures at higher Re_T determines a change in the scaling of the gas transfer rate.

Another crucial aspect of the surface flow, especially relevant for the transport of contaminants, is the relative velocity and dispersion of floating particles. This was investigated by Cressman *et al.* (2004) who found experimentally a retarded dispersion with respect to the super-diffusive regime proposed by Richardson (1926), while the latter was approximately recovered by numerical simulations. Recently, using a large-scale jet-stirred tank, we showed how the surface flow compressibility leads to anomalously large relative velocities at small separations, causing the ballistic regime of pair dispersion to extend over the inertial range of temporal separations (Li *et al.* 2024). This study was the first to reach a sufficient scale separation for the emergence of the classic power-law scaling of Kolmogorov's (1941) theory in the surface velocity field. However, the flow was imaged by following sparse floating particles, which did not allow us to resolve the dissipative scales.

An important aspect of free-surface flows in general, and the ones involving homogeneous bulk turbulence in particular, is represented by the effect of surface contamination. Herlina & Jirka (2008) presented seminal experimental measurements of near-surface flow velocity and dissolved gas concentration in a grid-stirred zero-mean-flow tank. Despite extensive measures taken to keep the surface clean, the horizontal velocity fluctuations decayed in the vicinity of the surface, signalling that trace amounts of surfactants caused a departure from an idealised zero-shear-stress boundary condition. Similar observations were made by Variano & Cowen (2013) in a jet-stirred zero-mean-flow tank. They stressed how the cleaning of the surface was instrumental to contain those effects, but that some contamination was unavoidable. The situation may be somewhat different in channel flows where the free surface is only exposed to the ambient air for a few seconds. However, even the careful channel flow study of Turney & Banerjee (2013) reported and discussed the evidence of trace amounts of surfactants altering the

surface motion. As those authors stated, residual amounts of surfactants 'seem almost impossible to remove fully' even in well-controlled laboratory experiments. Clearly, such trace amounts of surfactants are an important aspect of free-surface flows, especially those involving the spatial and temporal scales relevant for fully developed turbulence.

Although producing completely uncontaminated free-surface turbulence remains an unmet challenge, the value of well-controlled laboratory experiments cannot be overstated. The above-mentioned experiments by Herlina & Jirka (2008) provided clear evidence that, below a critical Reynolds number, the gas transfer velocity scales as $Re_T^{-0.25}$, in agreement with the model of Banerjee *et al.* (1968) and Lamont & Scott (1970). This was confirmed by numerical simulations by Herlina & Wissink (2014) where the idealised zero-contamination condition was applied. Later, Wissink *et al.* (2017) performed numerical simulations in which the level of surface contamination was modelled and systematically varied, and found that the scaling of the gas transfer velocity with Re_T was unaltered. What was strongly affected was its scaling with the Schmidt number Sc, related to Marangoni effects. They showed that even small levels of contamination would lead to a reduction of horizontal velocity fluctuations at the surface. Additionally, they found that the gas transfer scaling with Sc derived in the absence of surfactants was no longer accurate in the presence of even slight contamination. As discussed above, numerical simulations of this class of flows necessarily apply simplifications. Beside imposing a strictly flat surface, Wissink *et al.* (2017) considered insoluble surfactants. The effect of soluble surfactants may be qualitatively different (Tsai & Yue 1995). In fact, recent experiments on surface waves have found that the extended exposure of the surface to ambient air has similar effects to the presence of soluble surfactants (Erinin *et al.* 2023).

The above clearly indicates how, despite the importance of fine-scale flow features for a wealth of relevant processes, the detailed topology and dynamics of free-surface turbulence have not been sufficiently documented to comprehensively describe their behaviour. This is in stark contrast with 3-D turbulence, for which the properties of the velocity-gradient tensor and velocity differences over dissipative and inertial scales, as well as their role in the dynamics, have been explored in great depth in both the Eulerian and the Lagrangian frames (Sreenivasan & Antonia 1997; Meneveau 2011; Johnson & Wilczek 2024). Therefore, many fundamental questions remain to be clarified: What are the spatial and temporal scales associated with the divergence, vorticity and strain rate of the surface flow? Does the classic scaling of velocity differences hold in free-surface turbulence? How do the upwelling and downwelling events affect the dynamics, particularly the surface vorticity and strain rate? Addressing those and related questions is crucial, e.g. to devise effective coarse-grained representations of the surface flow, in particular considering the vast range of scales at play in nature.

Here, we conduct and analyse an experimental campaign in which the free-surface flow above homogeneous turbulence is characterised using particle tracking velocimetry (PTV). By imaging microscopic floating particles at high spatial and temporal resolution, we capture velocity gradients along dense trajectories, which allows us to gain a comprehensive view of the processes. The paper is organised as follows. In § 2, the experimental set-up and methodology are introduced, and the considered flow regime is described. In § 3, kinematic relations between the surface divergence, vorticity and strain rate are derived (§ 3.1); those quantities are described in terms of single-point statistics (§ 3.2) and structure topology (§ 3.3). The two-point/two-time statistics are presented in terms of velocity structure functions (§ 3.4), Eulerian and Lagrangian autocorrelations (§ 3.5) and cross-correlations (§ 3.6). The clustering of floating particles is discussed in § 3.7. We summarise our findings and draw conclusions in § 4.

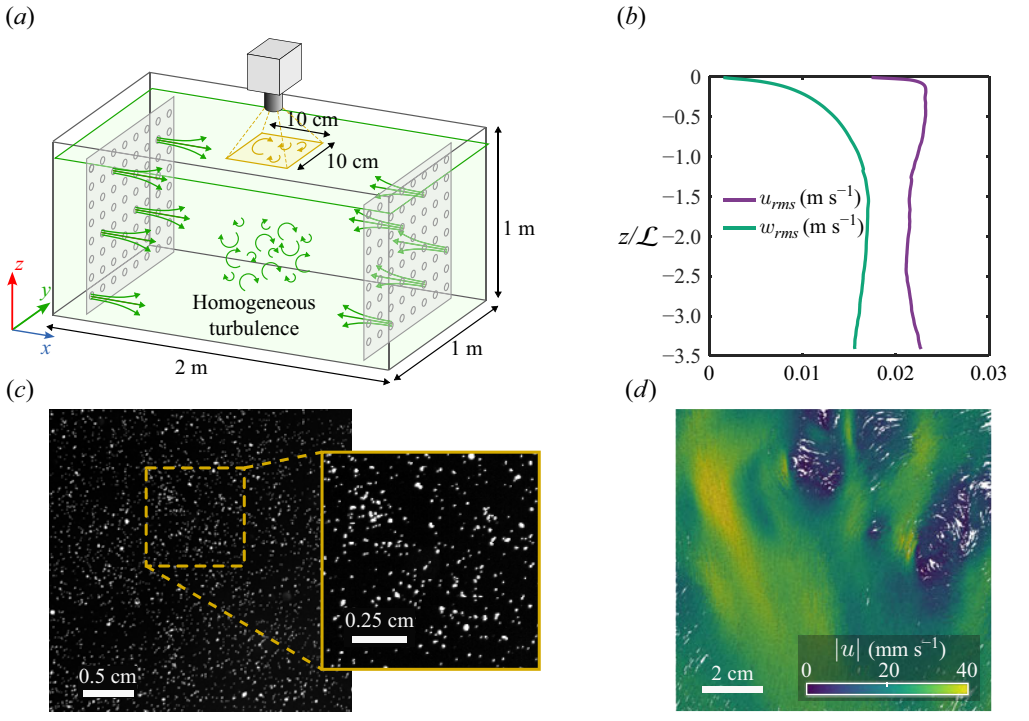

Figure 1. (*a*) A schematic of the turbulent water tank and camera arrangement. The yellow shaded area represents the FOV. (*b*) Profiles of surface-parallel and surface-normal r.m.s. fluctuation velocity (u_{rms} and w_{rms}, respectively) along the vertical direction. (*c*) A portion of a snapshot illustrating the floating micro-particles. (*d*) An example of surface trajectories at $Re_\lambda = 312$, colour coded by the velocity magnitude $|\boldsymbol{u}|$.

2. Experimental set-up and method

2.1. *Experimental set-up*

Experiments are conducted in a turbulent water tank as illustrated in figure 1(*a*). The tank has dimensions of $2 \times 1 \times 1$ m^3. In this tank, two 8×8 arrays of submerged pumps are placed against each other, with adjacent pumps separated by 10 cm in the horizontal and vertical directions. These pumps are controlled by programmable logic controllers and are turned on and off in a random pattern following the algorithm proposed by Variano & Cowen (2008). On average, one in eight pumps is on at any given time and each jet emission lasts 3 s. The turbulence generated in the centre of the tank is approximately homogeneous over a region of approximately 0.5 m^3. The intensity of the velocity fluctuations and the dissipation rate of the turbulent kinetic energy ϵ can be adjusted by changing the power supplied to each pump. We denote with x and y the horizontal directions parallel and perpendicular to the pump axes, respectively, and with z the vertical upward direction, the origin being at the free surface; u, v and w are the respective components of the velocity vector $\boldsymbol{u}$. Further details regarding the facility can be found in Ruth & Coletti (2024) and Li *et al.* (2024).

The water level is 8 cm (which is around one integral scale) above the axis of the top row of jets. This is significantly smaller compared with most previous experiments in which the turbulence was forced at depth (Brumley & Jirka 1987; McKenna & McGillis 2004; Herlina & Jirka 2008; Variano & Cowen 2008, 2013). Therefore, as discussed in Ruth & Coletti (2024), the spatial decay of turbulence away from the forcing region is

marginal and the evolution of the flow in the z direction is mostly caused by the free-surface boundary condition. The latter impacts especially the surface-normal component of the velocity, as illustrated in figure 1(*b*), which shows vertical profiles of surface-normal and surface-parallel r.m.s. velocity fluctuations (w_{rms} and u_{rms}, respectively) obtained and described by Ruth & Coletti (2024) using particles image velocimetry (PIV). During the experiment, the surface remains essentially flat, with deformation amplitude <0.5 mm as measured by planar laser-induced fluorescence (Ruth & Coletti 2024). The surface is periodically skimmed to avoid accumulation of surfactants, and a surface tension of $0.07\,\mathrm{Ns}^{-1}$ is measured using a Du Noüy ring at various points in time without seeding particles. We note that the results presented in this work are not sensitive to the exact time between the skimming and measurements, and they are robust once the free surface is recently skimmed. Still, the effect of residual surfactants is visible in the decay of the surface-parallel fluctuations approaching the surface. Similar trends were observed by Variano & Cowen (2013) despite their efforts in cleaning the surface. Complete removal of the residual surfactant requires chemical processes; their effect, however, would not last a sufficiently long time for the completion of the present measurements.

As illustrated in figure 1(*a*), a downward looking CMOS camera is placed approximately 0.31 m above the surface to capture the surface motion within a 10×10 cm^2 field of view (FOV) illuminated by two LED panels. The camera has a resolution of 1664×1600 pixels and is operated at 400 frames per second. The fluid motion on the surface is characterised by seeding 63–75 μm floating polyethylene microspheres with a density of 0.31 g cm^{-3}. To resolve the small-scale structures, the concentration of particles is maintained at approximately 120 particles cm^{-2}, leading to a mean inter-particle separation of around 1 mm. As the particles have a narrow size distribution and their mutual distance is much larger than their diameter, aggregation is minimised and individual particles can be clearly identified and tracked (figure 1*c*). This is done using an in-house PTV code based on the nearest-neighbour algorithm (Petersen *et al.* 2019). Given the particle trajectories, the velocity is obtained by convolving the trajectories with the first derivative of a temporal Gaussian kernel. The width of the kernel is determined following the approach by Mordant *et al.* (2004), and the resulting width (35–55 frames) is comparable to the smallest time scales of the flow. An example of trajectories in the FOV over 25 frames is shown in figure 1(*d*).

2.2. *Velocity-gradient calculation*

In order to probe the small-scale structure on the free surface, the surface velocity gradient $\nabla_s \boldsymbol{u}$ is calculated, where $\nabla_s = (\partial/\partial x)\boldsymbol{i} + (\partial/\partial y)\boldsymbol{j}$ is the surface gradient with $\boldsymbol{i}$ and $\boldsymbol{j}$ being the unit vectors along the x and y directions, respectively. For a given particle located at $\boldsymbol{x}^0$ on the free surface, the velocity of surrounding particles located at $\boldsymbol{x}^p$ within a search radius R_s around $\boldsymbol{x}^0$ can be approximated by the leading terms in the Taylor expansion

$$\boldsymbol{u}(\boldsymbol{x}^p) \approx \boldsymbol{u}(\boldsymbol{x}^0) + \nabla_s \boldsymbol{u}(\boldsymbol{x}^0)(\boldsymbol{x}^p - \boldsymbol{x}^0), \tag{2.1}$$

with $p = 1, \ldots, n$. The value of $\nabla_s \boldsymbol{u}$ at $\boldsymbol{x}^0$ is uniquely determined from (2.1) when two surrounding particles are found. In the case of more than two surrounding particles, $\nabla_s \boldsymbol{u}$ is calculated by minimising the squared residuals $\sum_p \left[\boldsymbol{u}(\boldsymbol{x}^p) - \boldsymbol{u}(\boldsymbol{x}^0) - \nabla_s \boldsymbol{u}(\boldsymbol{x}^p - \boldsymbol{x}^0)\right]^2$ (Pumir *et al.* 2013; Qi *et al.* 2022). We note that large R_s leads to a coarse-grained velocity-gradient tensor while small R_s may cause larger uncertainty as only a limited number of surrounding particles can be found. Here, R_s is thus selected following a similar approach to the one used to determine the width of Gaussian kernel in PTV: R_s is chosen as the

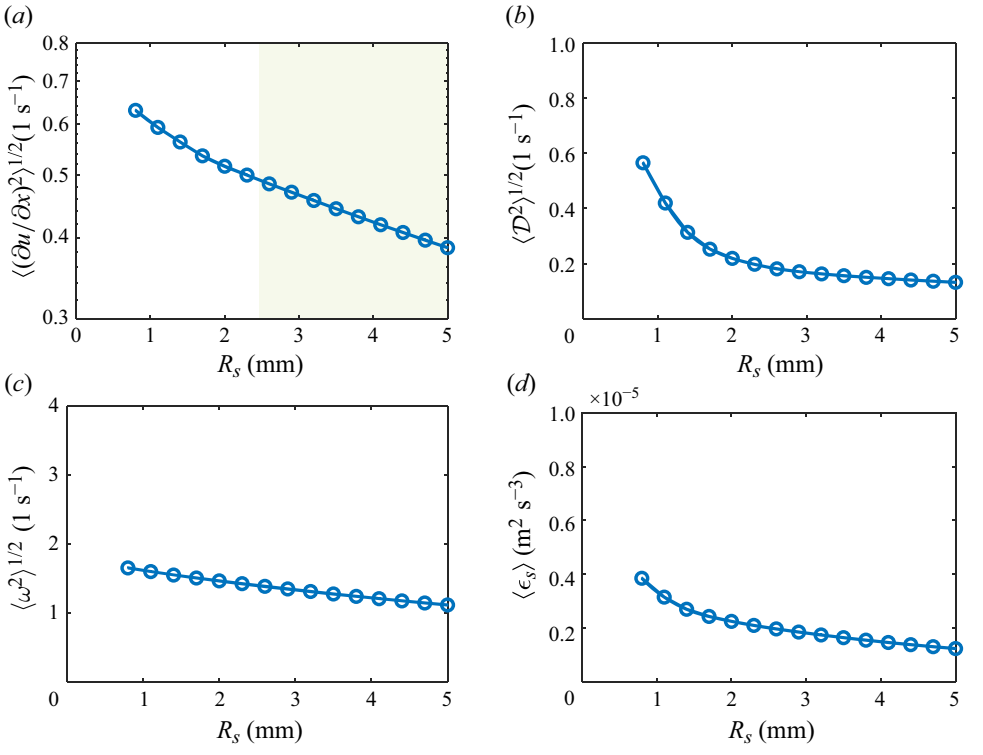

Figure 2. The evolution of different quantities as a function of the search radius R_s: (*a*) the standard deviation of one component of the velocity-gradient tensor $\langle(\partial u/\partial x)^2\rangle^{1/2}$; (*b*) the standard deviation of divergence $\langle\mathcal{D}^2\rangle^{1/2}$; (*c*) the standard deviation of vorticity $\langle\omega^2\rangle^{1/2}$; (*d*) mean dissipation rate on the surface $\langle\epsilon_s\rangle$. The green shading in panel (*a*) marks the range of exponential decay ($R_s > 2.5$ mm).

smallest value above which the standard deviation of $\nabla_s \boldsymbol{u}$ exhibits exponential decay, as shown figure 2(*a*). Following this method, we use $R_s = 2.5$ mm, yielding on average 40 particles within the search radius. As shown in figure 2(*b–d*), the key differential quantities evaluated along the surface, such as vorticity, dissipation rate and divergence, are only weakly sensitive to the exact choice of the search radius. In this work, to further minimise the uncertainty, velocity gradients calculated based on less than 5 particles are excluded from the statistics.

2.3. *Turbulence properties*

We consider four cases in which turbulence of different intensity is forced. Table 1 summarises the key parameters of the turbulence in the bulk as characterised by PIV, including the Kolmogorov length scale η and time scale τ_η, as well as the Taylor-microscale Reynolds number Re_λ. Moreover, to illustrate to which degree the surface flow approximates HIT, we calculate from the surface PTV data the homogeneity deviation $\mathrm{HD} = 2\sigma_{u'}/u'$, the isotropy factor $\mathrm{IF} = \langle(\partial u/\partial x)/(\partial v/\partial y)\rangle$ and the mean strain-rate factor $\mathrm{MSRF} = \langle(\partial\ \langle u\rangle\ /\partial x)/\langle(\partial u/\partial x - \partial\ \langle u\rangle\ /\partial x)^2\rangle^{\frac{1}{2}}\rangle$. Here, $\sigma_{u'}$ is the standard deviation of the spatial field of u' (Carter *et al.* 2016; Esteban *et al.* 2019), and angled brackets indicate ensemble averaging. The levels of HD and IF indicate a high level of spatial homogeneity and small-scale isotropy for all considered cases, while the small MSRF demonstrates that the mean velocity gradients are negligible compared with the instantaneous ones.

Re_λ	Re_T	ϵ (m^2 s^{-3})	η (mm)	τ_η (s)	$\mathcal{L}$ (m)	HD	IF	MSRF	$\mathcal{C}$
207	2630	3.82×10^{-5}	0.40	0.16	0.072	0.26	1.00	0.056	0.013
248	3427	8.31×10^{-5}	0.33	0.11	0.076	0.24	1.00	−0.047	0.015
283	4292	1.44×10^{-4}	0.29	0.08	0.080	0.21	0.98	0.064	0.020
312	5224	2.21×10^{-4}	0.26	0.07	0.083	0.18	1.00	0.012	0.024

Table 1. The main turbulence properties for the considered cases. The Taylor-microscale Reynolds number Re_λ, the large-scale Reynolds number Re_T, the dissipation rate ϵ, the Kolmogorov length scale η and time scale τ_η and the integral length scale $\mathcal{L}$ are evaluated in the bulk. The homogeneity deviation HD, the small-scale isotropy factor IF, the mean strain-rate factor MSRF and the compressibility coefficient $\mathcal{C}$ are defined in the text and are evaluated on the free surface.

3. Results

3.1. *Kinematic relation for energy dissipation rate on the free surface*

We first consider the mutual relations between vorticity, strain rate and divergence of the surface velocity field. The surface divergence $\mathcal{D}$ is defined as

$$\mathcal{D} = \nabla_s \cdot \boldsymbol{u} = \partial u/\partial x + \partial v/\partial y. \tag{3.1}$$

Considering the incompressibility of the fluid, $\mathcal{D}$ can also be expressed by $\mathcal{D} = -\partial w/\partial z$. Given the no-penetration boundary condition, $w = 0$ at $z = 0$ (which is approximately valid in the present case of weak surface deformation), positive/negative divergence represents upwelling/downwelling events. The vorticity and the strain rate on the free surface are, respectively,

$$\omega = \nabla_s \times \boldsymbol{u} = \partial v/\partial x - \partial u/\partial y, \tag{3.2}$$

and

$$s = \sqrt{\boldsymbol{S}_s \boldsymbol{S}_s}, \tag{3.3}$$

where $\boldsymbol{S}_s = \left[\nabla_s \boldsymbol{u} + (\nabla_s \boldsymbol{u})^T\right]/2$ is the symmetric 2-by-2 strain-rate tensor associated with the 2-D velocity field along the surface.

To connect the surface dynamics with the local properties of turbulence, the energy dissipation rate on the free surface also examined, i.e. $\epsilon_s = 2\nu \langle \boldsymbol{S}\boldsymbol{S} \rangle$. Note that, here, $\boldsymbol{S} = \left[\nabla \boldsymbol{u} + (\nabla \boldsymbol{u})^T\right]/2$ is the full 3-by-3 strain-rate tensor. As ϵ_s is evaluated along the free surface, the boundary conditions allow significant simplifications. In particular, considering that the free surface is quasi-flat, w is identically zero along the surface. This leads to $\partial w/\partial x = \partial w/\partial y = 0$. Also, the zero-stress boundary condition imposes $\partial u/\partial z = \partial v/\partial z = 0$. Therefore the (1, 2), (1, 3), (2, 1) and (3, 1) components of both $\nabla \boldsymbol{u}$ and $\boldsymbol{S}$ are zero. It follows that ϵ_s can be written as

$$\epsilon_s = 2\nu \left(\langle \boldsymbol{S}_s \boldsymbol{S}_s \rangle + \langle \mathcal{D}^2 \rangle \right) = 2\nu \left(\langle s^2 \rangle + \langle \mathcal{D}^2 \rangle \right). \tag{3.4}$$

We note that, in the current experiment, due to residual surfactant after skimming the surface (as mentioned above), the zero-stress boundary condition might not be strictly achieved. Therefore, ϵ_s calculated based on (3.4) might be weaker compared with a surface completely devoid of surfactants. Assessing this deviation, however, is difficult based on the surface PTV and is beyond the scope of this study. Equation (3.4) can be further expanded and rewritten as the summation of the quadratic terms of velocity gradient

$$\epsilon_s = 2\nu \left\langle 4 \left(\frac{\partial u}{\partial x} \right)^2 + \left(\frac{\partial u}{\partial y} \right)^2 + 3 \frac{\partial u}{\partial x} \frac{\partial v}{\partial y} \right\rangle. \tag{3.5}$$

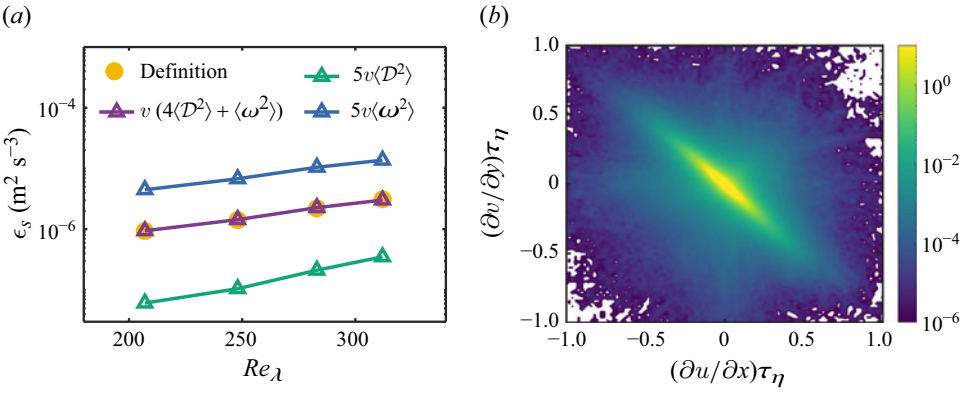

Figure 3. (*a*) The comparison of turbulence energy dissipation rate on the free surface ϵ_s calculated based on the definition (yellow symbols), (3.8) (purple symbols) and (3.9) (blue and green symbols). (*b*) The joint PDF of $\partial u/\partial x$ and $\partial v/\partial y$ normalised by the Kolmogorov time scale τ_η at $Re_\lambda = 312$.

Here, considering the properties listed in table 1, we have assumed the surface turbulence to be small-scale isotropic, which implies $\partial u/\partial x = \partial v/\partial y$ and $\partial u/\partial y = \partial v/\partial x$, and homogeneous, which implies $\langle(\partial u/\partial x)(\partial v/\partial y)\rangle = \langle(\partial u/\partial y)(\partial v/\partial x)\rangle$ (see equation 16 in George & Hussein (1991)). Those assumptions also allow us to write

$$\mathcal{D}^2 = 2\left(\frac{\partial u}{\partial x}\right)^2 + 2\frac{\partial u}{\partial x}\frac{\partial v}{\partial y}, \tag{3.6}$$

$$\omega^2 = 2\left(\frac{\partial u}{\partial y}\right)^2 - 2\frac{\partial u}{\partial x}\frac{\partial v}{\partial y}. \tag{3.7}$$

By comparing (3.5), (3.6) and (3.7), it is evident that ϵ_s can be rewritten following

$$\epsilon_s = \nu\left(4\langle\mathcal{D}^2\rangle + \langle\omega^2\rangle\right). \tag{3.8}$$

This kinematic relation, which allows expression of the dissipation rate along the surface from the strength of the divergence and vorticity on it, highlights the importance of the non-solenoidal nature and surface-attached vortices to the local properties of free-surface turbulence. In the case of vanishing divergence, this relation becomes the energy dissipation rate in incompressible 2-D turbulence $\epsilon_s = \nu\langle\omega^2\rangle$. Equation (3.8) agrees well with the present data for all considered cases, as shown in figure 3(*a*). The surface dissipation rate is found to be far smaller than the bulk value ϵ. This is consistent with previous theoretical and numerical studies (Teixeira & Belcher 2000; Guo & Shen 2010) in which a significant decrease of dissipation at the surface was found. The surface dissipation rate will be discussed further in § 3.4.

Equation (3.8) could be further simplified by assuming the compressibility ratio $\mathcal{C} = \langle(\nabla_s\cdot\boldsymbol{u})^2\rangle/\langle(\nabla_s\boldsymbol{u})^2\rangle = \langle\mathcal{D}^2\rangle/\langle(\nabla_s\boldsymbol{u})^2\rangle \approx 0.5$ as found in previous studies. Since this can also be expressed as $\mathcal{C} = \langle\mathcal{D}^2\rangle/[2\langle(\partial u/\partial x - \partial v/\partial y)^2\rangle]$ in the case of HIT, the condition $\mathcal{C} = 0.5$ is equivalent to a negligibly small correlation between $\partial u/\partial x$ and $\partial v/\partial y$ along the surface, i.e. $|\langle(\partial u/\partial x)(\partial v/\partial y)\rangle| \ll \langle(\partial u/\partial x)^2\rangle$ (Boffetta *et al.* 2004; Cressman *et al.* 2004). If this is assumed, the cross-product terms in (3.5), (3.6) and (3.7) are dropped and (3.8) simplifies to

$$\epsilon_s = 5\nu\langle\mathcal{D}^2\rangle = 5\nu\langle\omega^2\rangle. \tag{3.9}$$

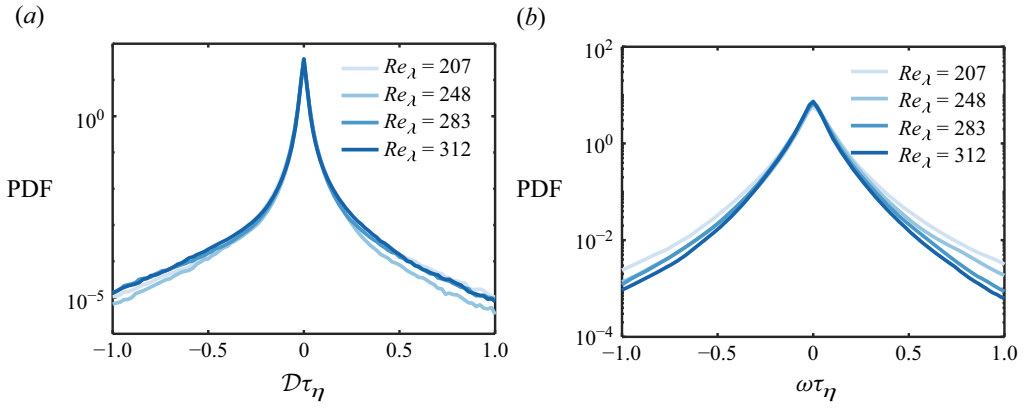

Figure 4. The PDFs of surface divergence $\mathcal{D}$ (panel (*a*)) and vorticity ω (panel (*b*)) at various Re_λ. In both panels, darker colour represents higher Re_λ and *vice versa*.

Figure 3(*a*), however, indicates that the data deviate considerably from this relationship. Indeed, the observed compressibility ratio (as reported in table 1) is much smaller than 0.5, which in turn is rooted in a strong correlation between $\partial u/\partial x$ and $\partial v/\partial y$. This is clearly illustrated in figure 3(*b*), which displays the joint probability density function (PDF) of $\partial u/\partial x$ and $\partial v/\partial y$ for the case $Re_\lambda = 312$, demonstrating strong anti-correlation between both quantities. This strong anti-correlation and the small compressibility ratio (as well as the weak surface divergence, which will be discussed in the following sections) might be influenced by residual surfactants on the free surface. The role of the latter, even in skimmed surface, was previously explored by Turney & Banerjee (2013). Here, and in the following, this Reynolds number will be used as exemplary case, and the behaviour of the other cases is analogous.

3.2. *Divergence, vorticity and strain rate*

Here, we examine the statistical distributions of the main velocity-gradient-based quantities characterising the surface flow: divergence, vorticity and strain rate. Figure 4(*a*) shows the PDF of divergence $\mathcal{D}$ non-dimensionalised by τ_η for the different Re_λ. The symmetric distributions indicate that the upwellings (associated with $\mathcal{D} > 0$) and the downwellings ($\mathcal{D} < 0$) occur with similar frequency and strength. The long tails signal strong intermittency, as previously observed (Schumacher & Eckhardt 2002; Cressman *et al.* 2004). In addition, the approximate collapse of the PDFs for the different Re_λ suggests that the statistical behaviour of the divergence follows a dissipative scaling. This is the case also for the PDFs of ω (figure 4(*b*)) which, however, display a far greater variance, i.e. $\langle \omega^2 \rangle \gg \langle \mathcal{D}^2 \rangle$. The relatively small magnitude of $\mathcal{D}$ is consistent with the small values of the compressibility coefficient, as discussed above. We remark that all components of the velocity-gradient tensor display symmetric distributions. This is in contrast with 3-D turbulence, where the skewness of the longitudinal velocity differences is associated with the direct energy cascade (Davidson 2015).

To examine the strain rate, figure 5(*a*) shows the PDFs of the eigenvalues λ_1 and λ_2 of $\boldsymbol{S}_s$, with $\lambda_1 > \lambda_2$. As $\boldsymbol{S}_s$ is a 2×2 symmetric tensor, both λ_1 and λ_2 are real numbers. The distributions of both eigenvalues are clearly antisymmetric. We remind the reader that, in 3-D turbulence, two out of three eigenvalues tend to be positive, which indicates bi-axial stretching (Betchov 1956; Davidson 2015). Cardesa *et al.* (2013) investigated the

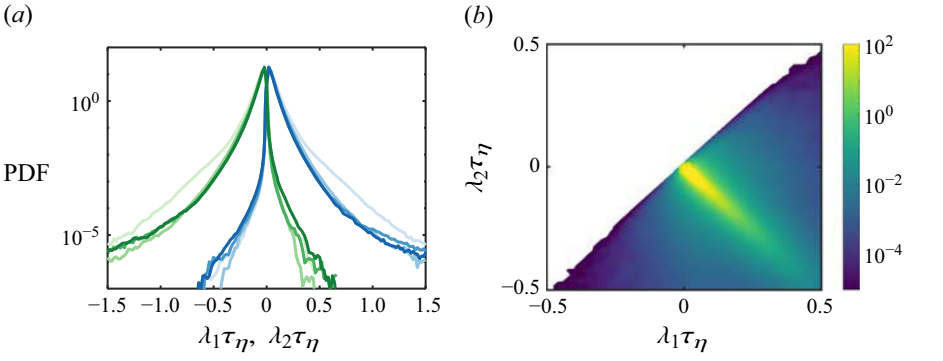

Figure 5. (*a*) The PDFs of the normalised eigenvalues λ_1 (blue lines) and λ_2 (green lines) of $\boldsymbol{S}_s$ at various Re_λ. Here, darker colour represents higher Re_λ and *vice versa*. (*b*) The joint PDF of λ_1 and λ_2 for $Re_\lambda = 312$.

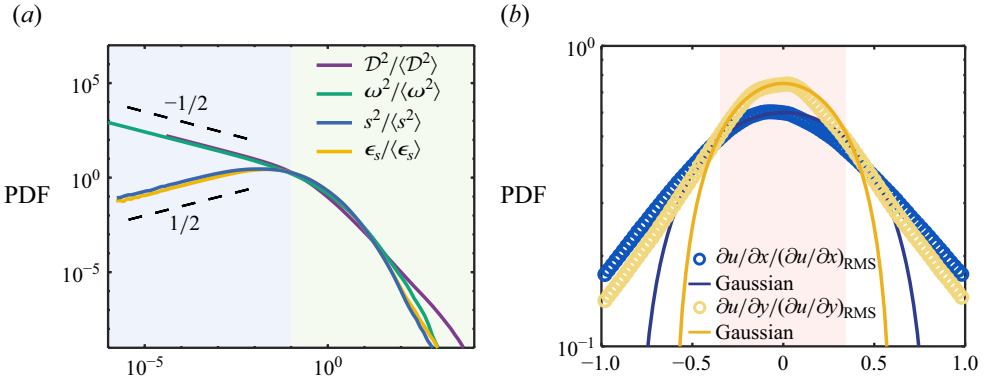

Figure 6. (*a*) The PDFs of normalised surface divergence square $\mathcal{D}^2$, vorticity square ω^2, strain-rate square s^2 and energy dissipation rate on the free surface ϵ_s. The dashed lines mark the scaling of power-law tails. The blue and green shaded areas illustrate the region where these quantities are smaller and larger than 10 % of their mean values, respectively. (*b*) The PDFs of two components of the velocity-gradient tensor $\partial u/\partial x$ (yellow symbols) and $\partial u/\partial y$ (blue symbols) normalised by their r.m.s. The solid lines show the fitted Gaussian distribution. The red shaded area from –0.3 to 0.3 marks the region where the PDFs are approximately Gaussian.

reduced strain-rate tensor and the two associated eigenvalues along 2-D sections of 3-D turbulence, finding predominance of compression over stretching. Along the free surface, on the other hand, compression and stretching appear equally likely and intense, similarly as the instances of positive and negative divergence (see figure 4*a*). The collapse of λ_1 and λ_2 for different Re_λ indicates that Kolmogorov scaling again applies, as for $\mathcal{D}$ and ω. The structure of the strain field is further clarified by the joint PDF of both eigenvalues displayed in figure 5(*b*), the other Reynolds numbers showing analogous behaviour. The strong anti-correlation indicates a high likelihood of $\lambda_1 \approx -\lambda_2$, i.e. comparable strength of compression and stretching along perpendicular directions. This is consistent with figure 3(*b*) displaying relatively small surface divergence, which can be expressed as $\mathcal{D} = \lambda_1 + \lambda_2$.

The magnitude of the different quantities is compared in figure 6(*a*), showing the PDFs of $\mathcal{D}^2$, ω^2, s^2 and ϵ_s, normalised by their mean value. In the range of low intensity events (blue shaded area), the distributions show power-law scaling with slopes of 1/2

for s^2 and ϵ_s, and $-1/2$ for $\mathcal{D}^2$ and ω^2. Power-law tails over the small-magnitude range were also observed for PDFs of squared vorticity and strain rate in 3-D turbulence by Yeung *et al.* (2012) and Carter & Coletti (2018), who explained them by the ansatz that small-velocity-gradient events behave as random variables. This is also the case here, as illustrated by figure 6(*b*), where PDFs of $\partial u/\partial x$ and $\partial u/\partial y$ are shown. It is evident that both quantities (and other components of the velocity gradient, not shown) approximately follow a Gaussian distribution when their magnitude is relatively small, e.g. less than 30 % of their r.m.s. values, as indicated in figure 6(*b*). As the quantities in figure 6(*a*) are summation of squares of velocity-gradient components, we expect them to follow chi-square distributions

$$P(X) \sim X^{k/2-1} e^{-X/2}, \tag{3.10}$$

where X is the variable representing $\mathcal{D}^2$, ω^2, s^2, and ϵ_s, k is the order of the chi-square distribution specifying the number of independent squared terms being summed and e is the natural exponent. For small X, this yields a power-law tail with a slope of $k/2-1$. For $\mathcal{D}^2$ and ω^2, only one squared term is involved with $k=1$, and the power-law slope $-1/2$ is retrieved. The squared strain rate can be written as $s^2 = (\partial u/\partial x)^2 + (\partial v/\partial y)^2 + (\partial u/\partial y + \partial v/\partial x)^2/2$, hence $k=3$, which yields the observed $1/2$ slope. Finally, the surface dissipation can be expressed by $\epsilon_s = 2\nu\left[s^2 + (\partial w/\partial z)^2\right]$, where $\partial w/\partial z$ is not an independent term considering the incompressibility condition. Therefore, $k=3$ is again obtained, and the scaling of the low-range tail of ϵ_s follows the one of s^2.

At the opposite end (green shaded area in figure 6*a*), we notice that the right tails of the PDFs of ω^2 and s^2 follow similar patterns. This was also observed in 3-D turbulence (Yeung *et al.* 2012), suggesting that intense events of strain and vorticity are concurrent. The distribution of ϵ_s essentially matches that of s^2, consistent with (3.4) which results in $\epsilon_s \approx 2\nu s^2$ for $\mathcal{C} \ll 1$. Although the divergence is in general relatively small, its intermittency is even higher than the other analysed quantities. The overall strong intermittency of the velocity gradient as well as its associated quantities on the free surface was recently found to be associated with the nonlinear self-amplification of the velocity gradient (Qi *et al.* 2025), which also accounts for the strong intermittency in 3-D turbulent flows (Meneveau 2011; Johnson & Wilczek 2024).

3.3. *Topology of small-scale structures*

We then examine the topology of small-scale structures; in particular, three sets of discrete structures used to characterise the spatial organisation of events of high surface divergence, vorticity and strain rate. Those structures are defined as contiguous regions satisfying the conditions $|\mathcal{D}| > \alpha_{\mathcal{D}} \langle \mathcal{D}^2 \rangle^{1/2}$, $|\omega| > \alpha_\omega \langle \omega^2 \rangle^{1/2}$ and $s > \alpha_s \langle s \rangle$, where $\alpha_{\mathcal{D}}$, α_ω and α_s are positive constants. To determine appropriate thresholds, we analyse the percolation behaviour of the intense structures as first proposed by Moisy & Jiménez (2004). For high threshold values, only a few small objects can be detected. As the threshold decreases, the objects grow in size and number and eventually start merging. The optimal threshold is obtained by identifying the intermediate value for which the objects are most numerous. This procedure was used extensively to identify structures in various configurations including channel flows (Lozano-Durán *et al.* 2012), free shear flows (Dong *et al.* 2017) and homogeneous turbulence (Carter & Coletti 2018).

Here, the velocity gradient measured at the position of each particle is first interpolated on a Cartesian grid with size equal to half the mean inter-particle distance. Figure 7(*a*) then shows how the number of detected objects varies as a function of threshold level, yielding the choice $\alpha_{\mathcal{D}} = 0.4$, $\alpha_\omega = 0.6$ and $\alpha_s = 1.5$. It is noted that the following results

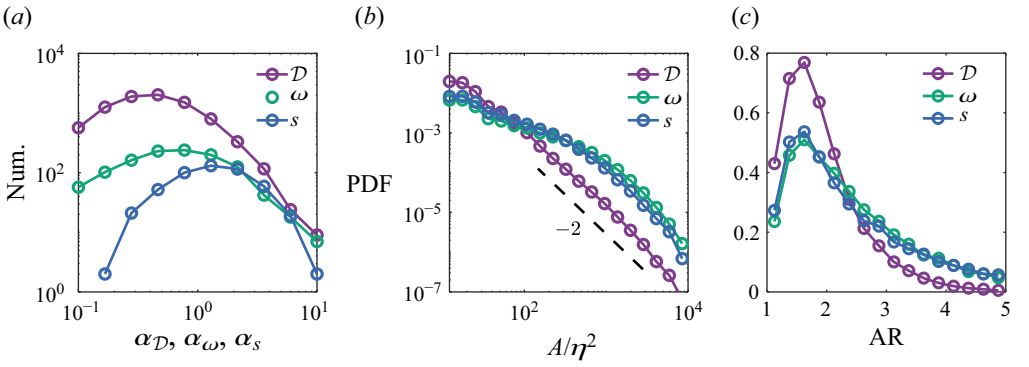

Figure 7. (*a*) The number of high-intensity objects found in the FOV as a function of thresholds. (*b*) The PDFs of the normalised area of high-intensity objects. The dashed line marks the power-law scaling of -2. (*c*) The PDFs of the aspect ratio of high-intensity events. In all of the panels, the purple, green and blue symbols represent high-divergence, high-vorticity and high-strain objects, respectively. Only the data for $Re_\lambda = 312$ are included.

are not sensitive to the exact values of thresholds. Moreover, objects that touch the FOV boundary are discarded. Although this may lead to underestimation of the number of large structures, it will be shown that the vast majority of the identified objects are much smaller than the FOV.

Figure 7(*b*) shows the PDFs of the area of high-divergence, high-vorticity and high-strain-rate structures, normalised by the Kolmogorov scale. The size of the structures is widely distributed over four decades. The high-vorticity and high-strain objects follow a similar trend, confirming the correlation between events of intense ω and s. These structures are on average larger compared with the regions of high divergence. Over some size range, the distributions appear compatible with a power-law decay, which may suggest a link with the scale-invariant properties of turbulence (Sreenivasan 1991; Moisy & Jiménez 2004; Carter & Coletti 2018). The limited range of scales over which this is evident, however, does not allow any conclusive statement in this sense.

In order to characterise the geometry of these structure, we also consider their aspect ratio $\mathrm{AR} = R_1/R_2$, where R_1 and R_2 are the major and minor axes of an ellipse that has the same second central moments as the structure. To ensure an accurate AR calculation, objects with area smaller than 5 grid cells (corresponding to around $5\eta^2$) are not considered in these statistics. It is found the results do not display discernible dependence on the cutoff value between 3 and 9 grid cells. Figure 7(*c*) shows the PDFs of AR for the three types of structures. Again, the curves for the high-vorticity and high-strain objects largely overlap. Those structures have generally larger AR, indicating that high-vorticity and high-strain-rate structures are more elongated compared with those of high divergence.

These properties are confirmed by the visual observations of instantaneous fields, samples of which are reported in figure 8(*a–c*): the high-divergence events are relatively small scale and spotty whereas the high-vorticity and high-strain regions are larger and more elongated. This divergence snapshot is consistent with the numerical simulation at a lower Reynolds number ($Re_T \approx 1800$) by Herlina & Wissink (2019), in which the surface divergence also appears to have a smaller length scale compared with the integral scale in the bulk. Moreover, the vorticity and strain-rate fields follow similar patterns, with high-vorticity magnitude (both positive and negative) events also overlapping with high-strain regions. This concurrence of intense vorticity and strain is also found in 3-D turbulence

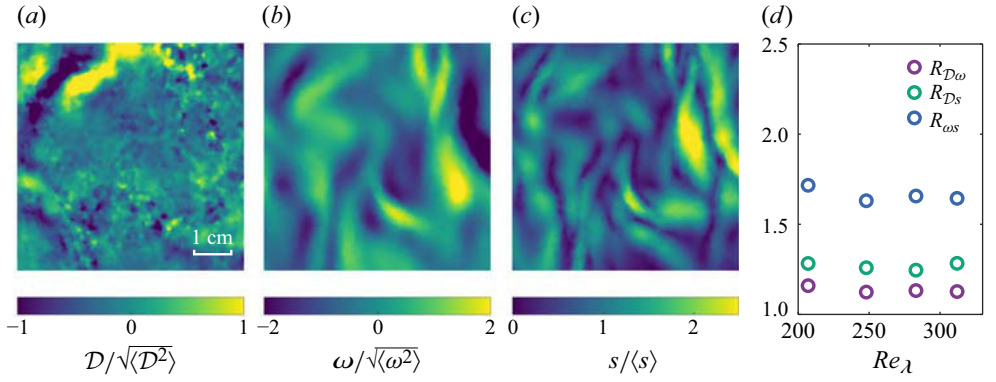

Figure 8. (*a–c*) Snapshots of surface divergence field (*a*), vorticity field (*b*) and strain field (*c*) on the free surface $Re_\lambda = 312$. (*d*) Overlap coefficients as a function of Re_λ. The purple, green and blue symbols represent divergence–vorticity, divergence–strain and vorticity–strain overlap, respectively.

(Yeung *et al.* 2015). To quantify the topological connection between such objects, we define the overlapping coefficients between $\mathcal{D}$, ω and s, based on a procedure similar to the one used by Berk & Coletti (2023). For example, the overlap between high-vorticity and high-divergence structures is characterised by

$$R_{\mathcal{D}\omega} = \frac{A_{FOV}\langle A_{\mathcal{D}\omega}\rangle}{\langle A_{\mathcal{D}} A_\omega\rangle}, \tag{3.11}$$

where A_{FOV} is the total area of the FOV. Here, $A_{\mathcal{D}}$ and A_ω are the area of high-divergence and high-vorticity regions, respectively and $A_{\mathcal{D}\omega}$ denotes the overlapping area between these regions. If both types of structures are spatially uncorrelated, $R_{\mathcal{D}\omega} = 1$. Similarly, the divergence/strain-rate and vorticity/strain-rate overlapping coefficients are defined as

$$R_{\mathcal{D}s} = \frac{A_{FOV}\langle A_{\mathcal{D}s}\rangle}{\langle A_{\mathcal{D}} A_s\rangle}, \tag{3.12}$$

$$R_{\omega s} = \frac{A_{FOV}\langle A_{\omega s}\rangle}{\langle A_{\omega} A_s\rangle}, \tag{3.13}$$

where $A_s$represents the area of high-strain structures, and $A_{\mathcal{D}s}$ and $A_{\omega s}$ are overlapping areas defined similarly. Figure 8(*d*) shows $R_{\mathcal{D}\omega}$, $R_{\mathcal{D}s}$ and $R_{\omega s}$ for the different Re_λ. In all cases, high-vorticity and high-strain structures show significant correlation, consistent with the previous observations. Here, $R_{\mathcal{D}\omega}$ and $R_{\mathcal{D}s}$ are much weaker than $R_{\omega s}$, but the high-divergence events are more likely to be concurrent with high strain rate than high vorticity.

3.4. *Second-order velocity structure functions*

After exploring the small-scale properties of the surface flow field, we consider how the turbulent kinetic energy is distributed across the spatial scales as described by the second-order longitudinal structure function. This is defined as

$$D_{LL} = \left\langle \left(u_r\left(\boldsymbol{x} + r\hat{\boldsymbol{e}}_r\right) - u_r\left(\boldsymbol{x}\right)\right)^2 \right\rangle, \tag{3.14}$$

where r is the separation distance, $\hat{\boldsymbol{e}}_r$ represents the unit vector along the separation and u_r is the velocity component in the same direction. Figure 9(*a*) shows D_{LL} as a function of r/η for the different Re_λ. In all cases, a clear scaling $D_{LL} \sim r^{2/3}$ is visible for $r/\eta > 20$,

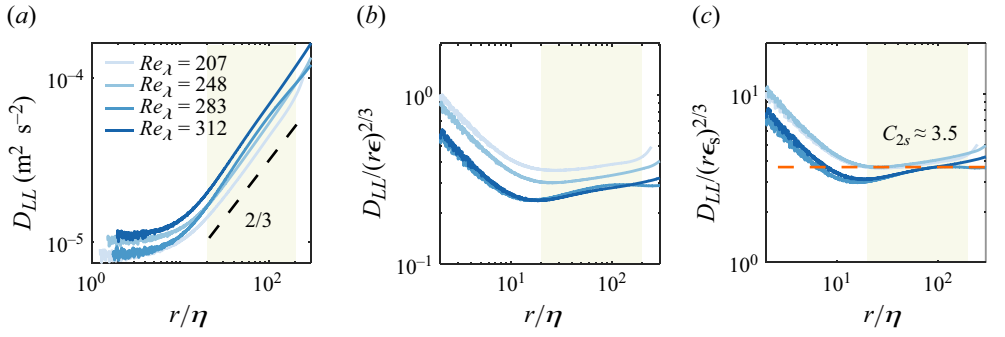

Figure 9. (*a*) The longitudinal second-order structure function D_{LL} as a function of the separation distance. The dashed line denotes 2/3 power-law scaling. (*b*) Value of D_{LL} normalised by $(r\epsilon)^{2/3}$. (*c*) Value of D_{LL} normalised by $(r\epsilon_s)^{2/3}$. The orange dashed line marks $C_{2s} \approx 3.5$. In all of the panels, the darker colour represents high Re_λ and *vice versa*. The green shaded area marks the inertial range.

consistent with the classic theory of Kolmogorov (1941) in the inertial sub-range. This was also observed in the laboratory experiments by Goldburg *et al.* (2001) and Cressman *et al.* (2004), and in outdoor water streams by Chickadel *et al.* (2011) (who reported the equivalent scaling of the energy spectrum with $k^{-5/3}$, k being the wavenumber) and by Sanness Salmon *et al.* (2023).

At smaller separations, the structure functions do not transition to the scaling $D_{LL} \sim r^2$ expected for smooth flows in the dissipation range, and instead their slopes become much shallower than in the inertial sub-range. This behaviour was recently reported by Li *et al.* (2024) using much sparser particle concentrations. Here, the finer spatial resolution allows us not only to confirm this finding, but also to reveal that the anomalously large relative velocities persist down to millimetric separations. As discussed in Li *et al.* (2024), this behaviour is similar to the formation of caustics in the velocity fields described by inertial particles in turbulence: such fields are also compressible, with intermittently large relative velocities and thus anomalous scaling exponents of the structure functions at small scales (Bec *et al.* 2010; Bewley *et al.* 2013; Berk & Coletti 2021; Bec *et al.* 2024). We note that, as the floating particles follow the fluid motion, their relative velocity must ultimately recover the scaling $u_r \sim r$ (and thus $D_{LL} \sim r^2$) in the limit of vanishing separations. This, however, may happen at scales only slightly larger than the particle diameter, not accessible even in the present high-resolution imaging system.

Besides the scaling with the separation r, a crucial prediction of Kolmogorov's theory is the dependence of the structure function with the dissipation in the inertial sub-range. In 3-D turbulence, the theory predicts $D_{LL} = C_2(\epsilon r)^{2/3}$, where $C_2 \approx 2.1$ is the Kolmogorov constant (Sreenivasan 1995). The compensated plots $D_{LL}/(\epsilon r)^{2/3}$ in figure 9(*b*) show that this relation does not hold in free-surface turbulence: the lines are not close to the value of 2.1 in the inertial range and, more importantly, they do not collapse. In fact, the dynamics on the free surface expected to be determined by the energy dissipation rate on the free surface ϵ_s rather than by the one in the bulk water ϵ. Indeed, the compensated plots $D_{LL}/(\epsilon_s r)^{2/3}$ in figure 9(*c*) show a much better collapse which indicates that the classic scaling still holds for free-surface turbulence when the dissipation rate on the surface is considered, i.e. $D_{LL} = C_{2s}(\epsilon_s r)^{2/3}$. Here, a distinct factor $C_{2s} \approx 3.5$ is obtained.

3.5. *Scales of surface divergence, vorticity and strain rate*

As seen in § 3.3, the surface divergence, vorticity and strain rate exhibit different length scales. This aspect is further investigated by examining the spatial autocorrelation

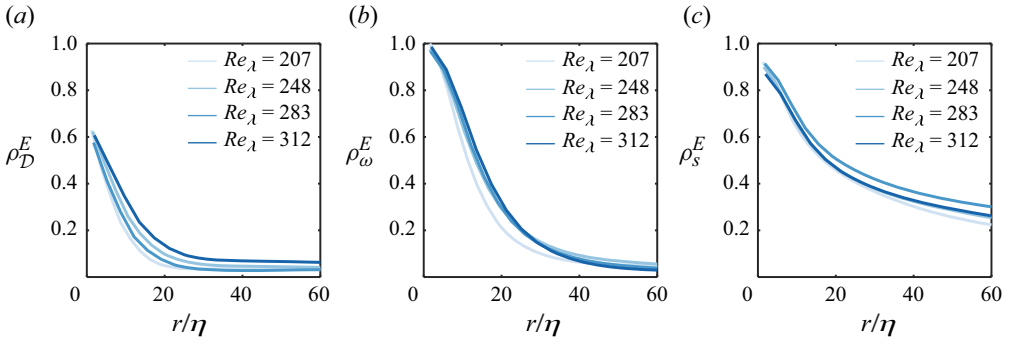

Figure 10. The Eulerian autocorrelation functions of divergence (*a*), vorticity (*b*) and strain (*c*) at different Re_λ. In all of the panels, the darker colour represents higher Re_λ.

functions of each quantity

$$\rho^E_{\mathcal{D}} = \frac{\langle \mathcal{D}'(\boldsymbol{x})\, \mathcal{D}'\left(\boldsymbol{x} + r\hat{\boldsymbol{e}}_r\right)\rangle}{\langle \mathcal{D}'^2\rangle}, \tag{3.15}$$

$$\rho^E_{\omega} = \frac{\langle \omega'(\boldsymbol{x})\, \omega'\left(\boldsymbol{x} + r\hat{\boldsymbol{e}}_r\right)\rangle}{\langle \omega'^2\rangle}, \tag{3.16}$$

$$\rho^E_{s} = \frac{\langle s'(\boldsymbol{x})\, s'\left(\boldsymbol{x} + r\hat{\boldsymbol{e}}_r\right)\rangle}{\langle s'^2\rangle}, \tag{3.17}$$

where the superscript E stands for Eulerian and the prime denotes fluctuations around the ensemble average. Figure 10 shows the autocorrelation for the various Re_λ. The divergence field (figure 10*a*) exhibits a characteristic length scale around (5–10)η, while the vorticity and strain-rate fields are characterised by somewhat larger correlation scales $\sim 20\eta$ and $\sim 30\eta$, respectively. This observation is consistent with the result in figures 7(*b*) and 8. Beyond some experimental scatter, the autocorrelation functions show no discernible dependence on Re_λ, with Kolmogorov scaling providing a fair collapse of the curves.

As the velocity gradient is obtained along floating particle trajectories, the temporal scales can also be investigated by calculating the temporal autocorrelation functions of divergence, vorticity and strain rate, respectively,

$$\rho^L_{\mathcal{D}} = \frac{\langle \mathcal{D}'(t)\mathcal{D}'(t+\tau)\rangle}{\langle \mathcal{D}'^2\rangle}, \tag{3.18}$$

$$\rho^L_{\omega} = \frac{\langle \omega'(t)\omega'(t+\tau)\rangle}{\langle \omega'^2\rangle}, \tag{3.19}$$

$$\rho^L_{s} = \frac{\langle s'(t)s'(t+\tau)\rangle}{\langle s'^2\rangle}. \tag{3.20}$$

Here, the superscript L stands for Lagrangian, t represents the generic temporal abscissa and τ is the time delay. Figure 11 shows the temporal autocorrelation functions for the different Re_λ, with the Kolmogorov scaling that again provides a reasonable collapse of the curves. The surface divergence shows a time scale comparable to τ_η, confirming it is driven by small-scale processes. On the other hand, the time scales of both vorticity and

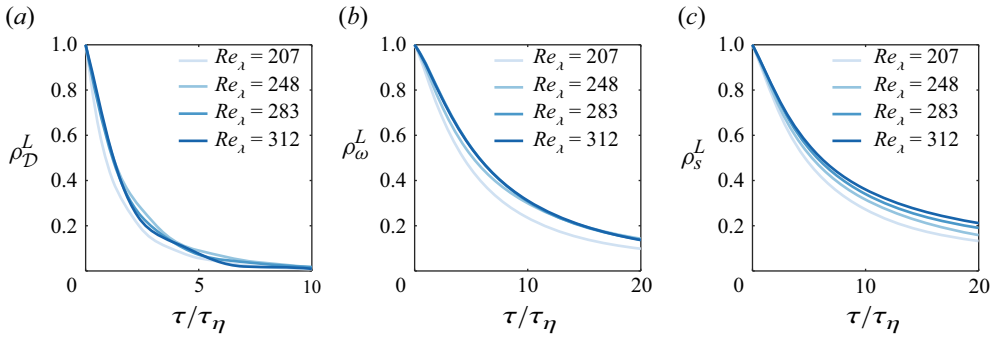

Figure 11. The Lagrangian autocorrelation functions of divergence (*a*), vorticity (*b*) and strain (*c*) at different Re_λ. In all of the panels, the darker colour represents higher Re_λ.

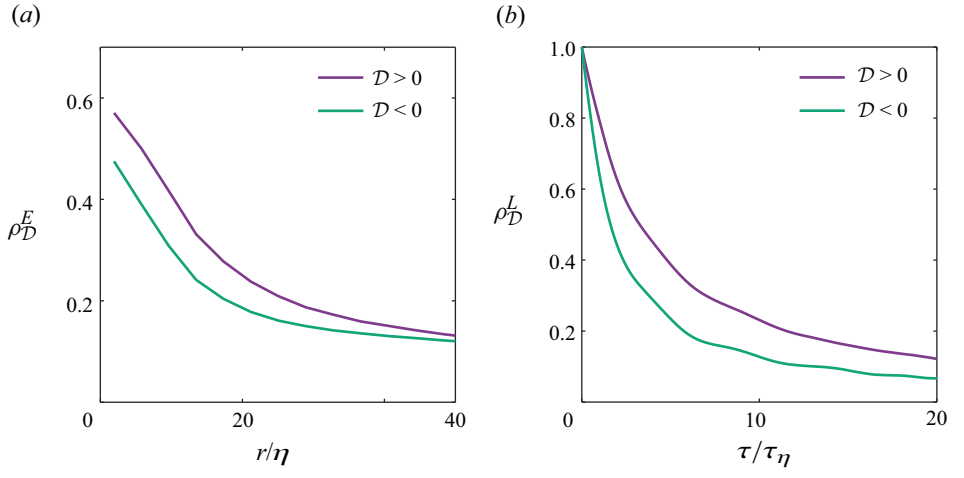

Figure 12. (*a*) The Eulerian autocorrelation functions for positive divergence (purple line) and negative divergence (green line). (*b*) The Lagrangian autocorrelation functions for positive divergence (purple line) and negative divergence (green line).

strain rate are significantly larger and comparable to the integral time scale, suggesting that surface-attached vortices and surface-parallel stretching and compression are long-lived compared with the lifetime of sources and sinks. These time scales, in fact, are also larger than their characteristic time scales in 3-D turbulence, which are expected to scale with τ_η.

Given the importance of the imbalance between upwellings and downwellings (Perot & Moin 1995; Guo & Shen 2010; Ruth & Coletti 2024), it is useful to distinguish between the scales associated with both types of events. Figures 12(*a*) and 12(*b*) plot the Eulerian and Lagrangian autocorrelation functions $\rho^E_{\mathcal{D}}$ and $\rho^L_{\mathcal{D}}$, respectively, conditioning on $\mathcal{D} > 0$ and $\mathcal{D} < 0$. It is clear that upwellings are associated with larger spatial and temporal scales along the surface flow compared with downwellings. This is consistent with the observation by Ruth & Coletti (2024) in the same facility and by Guo & Shen (2010) based on numerical simulations.

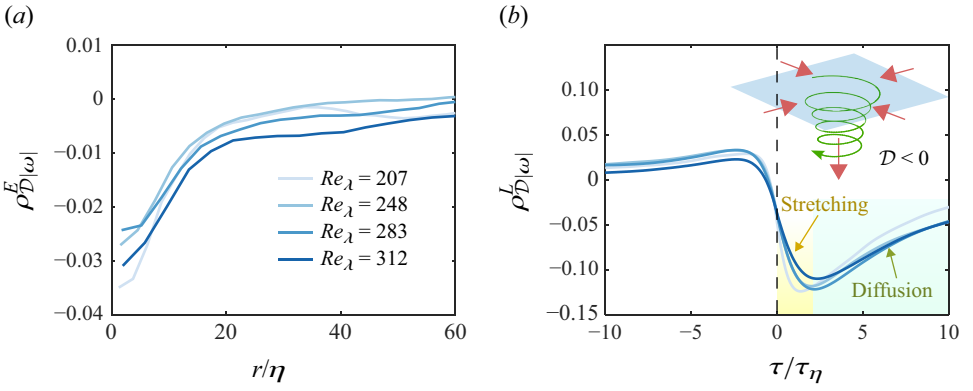

Figure 13. (*a*) The Eulerian cross-correlation functions between divergence and vorticity magnitude at different Re_λ. (*b*) The Lagrangian cross-correlation function between divergence and vorticity magnitude at different Re_λ. This panel shares the same legend with panel (*a*). The yellow shaded area marks the vortex-stretching process, and the green shaded area marks the diffusion process of surface-attached vortices. The schematic illustrates the vortex-stretching process. The green spiral marks the surface-attached vortex, the red arrows represent the negative divergence, and the blue plane shows the free surface.

3.6. *Cross-correlation among divergence, vorticity and strain rate*

Having characterised the spatial and temporal scales of divergence, vorticity and strain rate of the surface flow, we investigate its dynamics by considering the mutual correlation between those quantities, which will prove insightful towards a mechanistic understanding of the processes. We first consider the Eulerian cross-correlation between divergence and vorticity $\rho^E_{\mathcal{D}|\omega|}$

$$\rho^E_{\mathcal{D}|\omega|} = \frac{\langle \mathcal{D}'(\boldsymbol{x})\,|\omega|'\left(\boldsymbol{x} + r\hat{\boldsymbol{e}}_r\right)\rangle}{\langle \mathcal{D}'^2\rangle^{1/2}\langle |\omega|'^2\rangle^{1/2}}, \tag{3.21}$$

where the absolute value of the vorticity is used as the rotational direction of surface-attached vortices is immaterial. Figure 13(*a*) shows the cross-correlation for various Re_λ, with Kolmogorov scaling providing again a fair collapse of the different curves. For all cases, $\rho^E_{\mathcal{D}|\omega|} \approx -0.03$ at $r = 0$ is observed. This suggests that, although the correlation between these two quantities is weak, strong vorticity is more likely to be associated with negative surface divergence; i.e. surface-attached vortices are stronger when downwelling events occur. Moreover, figure 13(*a*) indicates a characteristic correlation scale $\approx 10\eta$. This is close to the length scale of the divergence as the latter decorrelates from itself faster than the vorticity (see figure 10).

To further probe the interaction between divergence and vorticity, we also examine the Lagrangian cross-correlation, which is defined as

$$\rho^L_{\mathcal{D}|\omega|} = \frac{\langle \mathcal{D}'(t)|\omega|'(t+\tau)\rangle}{\langle \mathcal{D}'^2\rangle^{1/2}\langle |\omega|'^2\rangle^{1/2}}. \tag{3.22}$$

As shown in figure 13(*b*), this cross-correlation remains around zero before $\tau < 0$, suggesting that strong vorticity events do not affect the divergence at later times. However, for $\tau \geqslant 0$, $\rho^L_{\mathcal{D}|\omega|}$ becomes negative and dips during a few Kolmogorov time units. This anti-correlation between $\mathcal{D}$ and ω, corroborating the observation in figure 13(*a*), indicates that sinks in the surface flow are statistically associated with the enhancement of surface-attached vortices at a later time. This can be explained by considering the physical picture illustrated in the inset of figure 13(*b*): when a sink (marked by a red arrow) is

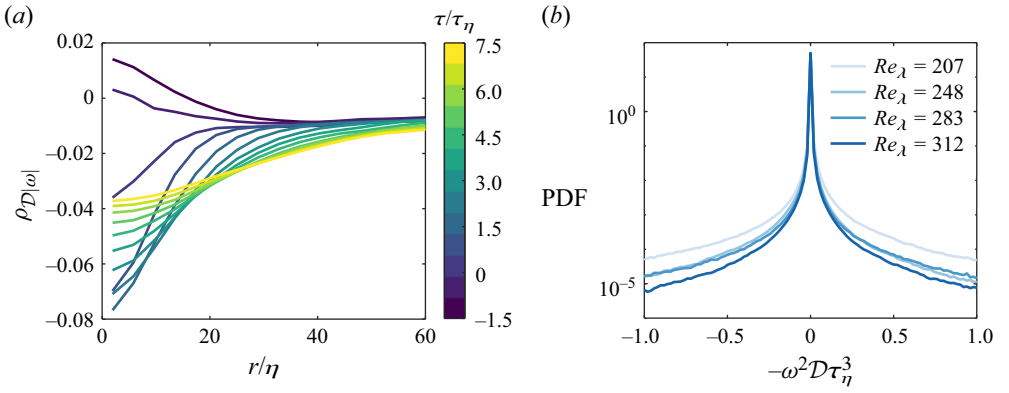

Figure 14. (*a*) The spatial-temporal cross-correlation between the divergence and vorticity magnitude as a function of separation distance. The colours represent the time delay τ. (*b*) The PDFs of the vortex-stretching term. The darker colour represent the higher Re_λ.

formed, the correspondent downwelling flow stretches downwards surface-attached vortex filaments (marked as a green spiral). As a result, the vorticity magnitude grows and $\rho^L_{\mathcal{D}|\omega|}$ decreases significantly (yellow shaded area in the plot). The typical duration of the vortex stretching, around $2\tau_\eta$, is consistent with the time scale of the events of negative divergence highlighted in figure 12(*b*). When the surface sink has dissipated, the vorticity diffuses and $\rho^L_{\mathcal{D}|\omega|}$ approaches zero (blue shaded area). We note that this picture should hold for different Re_λ, as indicated by the good collapse of the lines in figure 13(*b*).

This picture of the connection between vortex stretching and surface divergence is corroborated by figure 14(*a*), plotting the spatio-temporal cross-correlation between the divergence and vorticity

$$\rho_{\mathcal{D}|\omega|} = \frac{\langle \mathcal{D}'\,(\boldsymbol{x},t)\,|\omega|'\left(\boldsymbol{x}+r\hat{\boldsymbol{e}}_r,t+\tau\right)\rangle}{\langle \mathcal{D}'^2\rangle^{1/2}\langle |\omega|'^2\rangle^{1/2}}. \tag{3.23}$$

The cross-correlation is again weak for $\tau<0$; whereas, during the initial stage of the downwelling ($0<\tau<2\tau_\eta$), the vorticity intensifies and the cross-correlation dips into the negative range. The anti-correlation extends spatially to $r\approx 10\eta$, i.e. the characteristic length scale of the divergence; while after $\tau>2\tau_\eta$, when the sink dissipates, the diffusion of the vorticity leads to an increase of the cross-correlation length scale.

The connection between the surface divergence and surface-attached vortices has been explored by several authors. Banerjee (1994) proposed that a correlation must exist between the surface divergence and the number of surface-attached vortices, which was recently demonstrated by Babiker *et al.* (2023). Shen *et al.* (1999) used numerical simulations to provide a mechanistic interpretation of such correlation, showing how upwellings bring hairpin vortices close to the surface, where their surface-parallel section is dissipated, leaving vortex filaments that connect to the surface. The present analysis has emphasised the relation between surface vortices and downwellings, rather than upwellings. The former are naturally associated with vortex stretching, which in turn is classically attributed a key role in the energy cascade. However, the picture appears to be the completely different in free-surface turbulence, as we now show.

The evolution of vorticity under the action of the strain field is often characterised by examining the vortex-stretching term $\boldsymbol{\omega}\cdot\boldsymbol{S}\cdot\boldsymbol{\omega}$ in the enstrophy transport equation, where $\boldsymbol{\omega}$ is the vorticity vector. On the free surface, this term reduces to $\omega^2(\partial w/\partial z)=-\omega^2\mathcal{D}$.

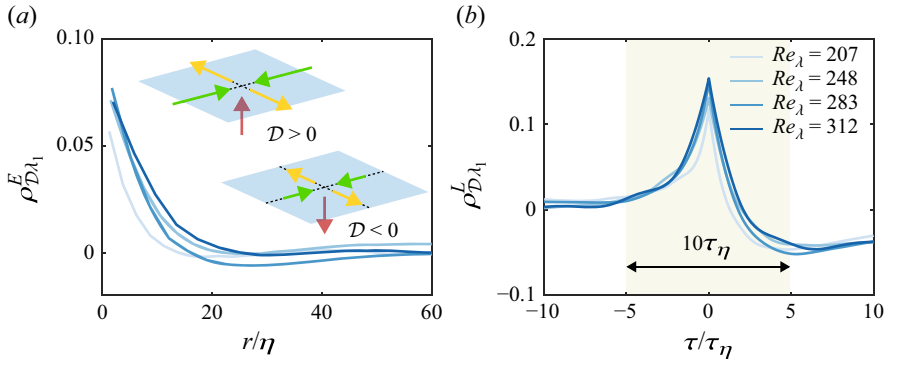

Figure 15. (*a*) The Eulerian cross-correlation function for the divergence and the larger eigenvalue of the strain-rate tensor on the surface λ_1 for different Re_λ. This panel shares the same legend with panel (*b*). The inset illustrates the relation between the positive/negative divergence (red arrows) and the strength of stretching (yellow arrows) and compression (green arrows) on the free surface. The length of the arrows marks the magnitude of stretching and compression. (*b*) The Lagrangian cross-correlation for the divergence and λ_1 for different Re_λ. The green shaded area which covers a time scale of $10\tau_\eta$ marks the time range when λ_1 increases and decreases.

Figure 14(*b*) shows the PDF of this terms normalised by Kolmogorov scales for all Re_λ. The distribution is symmetric and strongly intermittent. The symmetry is in stark contrast with the behaviour of 3-D turbulence, in which vortex stretching is predominant (Mullin & Dahm 2006; Buxton & Ganapathisubramani 2010; Bechlars & Sandberg 2017). The fact that the free surface ts to suppress the vortex stretching is also observed in Qi *et al.* (2025) by examining the asymmetry of the joint PDF of velocity-gradient invariants. This result may provide clues regarding the energy cascade along the free surface, which has been found to show inverse energy transfer from small to large scales (Pan & Banerjee 1995; Lovecchio *et al.* 2015).

As shown in § 3.3, the surface divergence is associated with vorticity as well as with strain rate, and in fact somewhat more significantly with the latter. To quantify this aspect, we consider the Eulerian cross-correlation between the surface divergence and λ_1

$$\rho^E_{\mathcal{D}\lambda_1} = \frac{\langle \mathcal{D}'(\boldsymbol{x})\, \lambda_1'\left(\boldsymbol{x} + r\hat{\boldsymbol{e}}_r\right)\rangle}{\langle \mathcal{D}'^2\rangle^{1/2}\langle \lambda_1'^2\rangle^{1/2}}. \tag{3.24}$$

Figure 15(*a*) plots this quantity for all cases, showing a positive correlation. This indicates that a larger positive surface divergence (stronger source) is likely to be associated with large (i.e. above average) strain rate along the surface stretching direction. As λ_1 and λ_2 are highly anti-correlated (see figure 5*b*), a compression of comparable magnitude is also likely to occur in the surface-parallel direction perpendicular to the one of stretching (with the compression slightly weaker than the stretching to satisfy incompressibility). This flow pattern is illustrated by the upper schematic in figure 15(*a*). On the other hand, a negative divergence is likely associated with weak (i.e. below average) strain rate along the surface accompanied by a weak compression perpendicular to it, as also sketched in the lower schematic of figure 15(*a*). The cross-correlation has a characteristic scale comparable to the length scale of divergence, similar as $\rho^E_{\mathcal{D}|\omega|}$ (figure 13*a*), although the magnitude of $\rho^E_{\mathcal{D}\lambda_1}$ is somewhat larger. This is consistent with the observation that divergent regions overlap slightly more with high-strain-rate regions compared with high-vorticity regions (figure 7*d*).

Finally, we examine the Lagrangian cross-correlation between divergence and λ_1 (figure 15*b*)

$$\rho^L_{\mathcal{D}\lambda_1} = \frac{\langle \mathcal{D}'(t)\lambda_1'(t+\tau)\rangle}{\langle \mathcal{D}'^2\rangle^{1/2}\langle \lambda_1'^2\rangle^{1/2}}. \tag{3.25}$$

Before a strong divergence event occurs (i.e. $\tau < 0$), $\mathcal{D}$ and λ_1 grow together, as indicated by the increasing correlation $\rho^L_{\mathcal{D}\lambda_1}$. Considering the strong anti-correlation between λ_1 and λ_2, this implies that the formation of a source is preceded by an increase in magnitude of the stretching–compression saddle along the surface. After λ_1 reaches its maximum at $\tau = 0$, it decreases and slowly approaches its mean with the stretching–compression saddle recovering to its average magnitude. For all Re_λ, the duration of significant correlation is approximately $10\tau_\eta$ (green shaded area), which is consistent with the lifetime of high-strain-rate events (figure 11*c*).

3.7. *Clustering on the free surface*

We finally examine the clustering of the floating particles along the surface. This process, originating from the compressible nature of the free surface, differs from the clustering of inertial particles in incompressible turbulence (Balachandar & Eaton 2010; Brandt & Coletti 2022). The latter results from the fact that inertial particles depart from the pathlines of fluid parcels whose fluctuations they cannot follow, thus leading to a compressible field (Maxey 1987). On the other hand, floating particles cannot follow the surface pathlines entering the bulk.

Figure 16(*a*) shows the radial distribution function (RDF) of floating particles defined as $g(r) = (N_r/A_r)/(N_t/A_{FOV})$, where N_r is the number of particles within a narrow circular ring with radius r and area A_r, and N_t is the total number of particles in the FOV. The RDF quantifies the local concentration around a generic particle, and thus values larger than unity indicate the formation of clusters over a certain length scale. In the present case, the values indicate moderate degree of clustering. This is compatible with the weak compressibility we observe. An exponential fit to the data yields a characteristic length scale of the clustering around 30η, close to the length scale $\sim 20\eta$ found in the simulations by Schumacher & Eckhardt (2002). The fact that the cluster length scale is significantly larger than that of divergence (figure 10*a*) suggests the clustering is also affected by the large-scale motion on the free surface. The inset of figure 16(*a*) displays the same RDF in logarithmic scale. While the range is not sufficient for a conclusive statement, the data are compatible with a power-law decay, which would indicate spatial self-similarity of the concentration field. This would be in turn consistent with previous works that show how floating particles cluster over fractal sets (Boffetta *et al.* 2006; Larkin *et al.* 2009).

The clustering of floating particles is also characterised using the Voronoi tessellation method (Monchaux *et al.* 2010). Figure 16(*b*) displays the PDF of the area of the Voronoi cells A_V for $Re_\lambda = 312$, compared with the PDF that approximates the distribution of scattered particles in a random Poisson process (Ferenc & Néda 2007). We note the data only cover a limited range down to $A_V/\langle A_V\rangle \approx 0.3$. This corresponds to 5×5 pixels in raw images, slightly larger than the particle size. Voronoi cells smaller than this criterion tend to have larger uncertainty. Nevertheless, the area PDF clearly shows higher probability at $A_V/\langle A_V\rangle < 0.83$ and $A_V/\langle A_V\rangle > 2$, indicating the occurrence of clusters and voids, respectively. The degree of clustering is quantified by calculating the standard deviation of the PDF, σ_{AV}, and comparing with that of the random Poisson process, $\sigma_{rpp} \sim 0.53$. The ratio $\sigma_{AV}/\sigma_{rpp} \sim 1.6$ confirms the moderate intensity of the clustering.

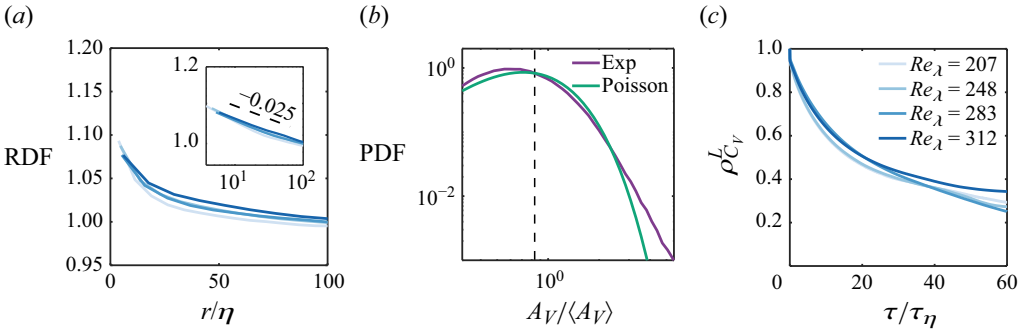

Figure 16. (*a*) The RDF of floating particles on the free surface for various Re_λ. The inset shows the same figure with the horizontal and vertical axes in logarithmic scales. This panel shares the same legend with panel (*c*). (*b*) The PDF of the area of Voronoi cells around floating particles for the case $Re_\lambda = 312$. The purple line shows the PDF for a random Poisson process. The black dashed line at $A_V/\langle A_V\rangle = 0.83$ marks the crossing point between both curves. (*c*) The Lagrangian autocorrelation of the partile concentration for various Re_λ.

The time scale of the clustering is further characterised by calculating its Lagrangian autocorrelation function

$$\rho^L_{C_V} = \frac{\langle C'_V(t)C'_V(t+\tau)\rangle}{\langle C'^2_V\rangle}, \tag{3.26}$$

as shown in figure 16(*c*), where $C_V = 1/A_V$ denotes the local concentration of particles. Results for different Re_λ collapse and exhibit a similar time scale around $\sim 40\tau_\eta$. This is significantly larger than the characteristic time scale of the divergence and is close to the integral time scale, highlighting again the role of the large-scale motions. This result is consistent with the observation by Lovecchio *et al.* (2013), who reported clusters evolving over a time scale similar to and even larger than the integral time scale of the underlying turbulence.

It is worth mentioning that, although the formation of clusters is associated with the compressible surface velocity field, the distribution of clusters is not expected to exhibit a strong connection with the instantaneous divergence field. Instead, clusters (voids) emerge where persistent sinks (sources) are present, i.e. the time history of the surface divergence needs to be considered. This mechanism potentially elucidates the distinct temporal and spatial scales exhibited by the clusters compared with the divergence.

4. Conclusions

In this work, we experimentally studied the small-scale dynamics of the free surface above homogeneous and isotropic turbulent water. We focus on a regime of negligible surface deformation. The experiment is conducted in a zero-mean-flow turbulent water tank in which the turbulence is forced by two opposingly placed jet arrays. A Taylor Reynolds number $Re_\lambda = 207$–312 is achieved and high-speed/high-resolution imaging is used to measure the free-surface flow. By seeding high-concentration floating particles, the surface velocity field is obtained by PTV and the velocity-gradient tensor is calculated along each trajectory by a local least-square approach.

We first derive a kinematic relation for the energy dissipation rate on the free surface. By applying the free-surface boundary conditions and assuming small-scale homogeneity and isotropy of the flow, the dissipation rate can be written as a function of surface divergence

and vorticity, highlighting its connection with the non-solenoidal nature of the surface and surface-normal vorticity.

The PDFs of divergence, vorticity and strain rate collapse once normalised by the Kolmogorov scales over the considered range of Re_λ. The symmetry of the PDF of divergence indicates that sources and sinks have similar strengths. The two eigenvalues of the strain-rate tensor show clear anti-symmetry and anti-correlation, suggesting the stretching and compression along the free surface are equally likely and intense, in contrast with the 3-D turbulence case in which stretching is predominant. The magnitude of these quantities is examined by plotting PDFs of the squares of them, in which power-law tails at small magnitude are evident. We show that this is due to the Gaussian core of the velocity-gradient PDF. As a result, these squared quantities follow chi-square distribution of different orders based on their definitions.

The intense-divergence, intense-vorticity and intense-strain-rate structures are identified by a percolation technique. The PDFs of the area of the structures show power-law scaling (although over a limited size range) suggesting that these structures are self-similar. The intense-divergence structures have smaller area, whereas the intense-vorticity and intense-strain structures are more elongated. These observations are further confirmed by their instantaneous fields. Moreover, strong overlap between the intense-vorticity and intense-strain regions is also observed.

To examine the energy at different scales, the second-order structure function along the free surface considered. A clear $r^{2/3}$ scaling is evident, consistent with the classic Kolmogorov theory. The scaling for the dissipation rate, on the other hand, is only preserved when the energy dissipation rate on the free surface used, i.e. $D_{LL} \sim \epsilon_s^{2/3}$. This leads to a factor $C_{2s} \approx 3.5$ which deviates from the one for 3-D turbulence. The plateau of D_{LL} at millimetric separation signals anomalously large relative velocities which are attributed to the compressible nature of the free-surface flow.

The scales of divergence, vorticity and strain are examined by calculating the Eulerian and Lagrangian autocorrelation functions. The results collapse after normalising by Kolmogorov scales. The time scale and length scale of divergence are close to Kolmogorov scales, suggesting the divergence is driven by small-scale processes. On the other hand, the vorticity and strain rate have larger length scales and are much longer lived compared with divergence. This behaviour emphasises the difference between the free-surface turbulence and 3-D turbulence, in which the time scales of vorticity and strain rate are of the order of the Kolmogorov time scale.

The mutual correlation among the divergence, vorticity and strain rate is explored by calculating the cross-correlation functions. Negative divergence events (sinks) are found to increase the magnitude of vorticity through a vortex-stretching process during which the surface-attached vortex is stretched by the downwelling. After this downwelling dissipates, the vortex diffuses and the vorticity decays. The evolution of the surface vorticity is characterised by the term $\omega^2\mathcal{D}$, whose PDF is symmetric, in stark contrast with 3-D turbulence where vortex stretching prevails. Moreover, upwelling events are likely to be associated with strong stretching/compression saddles along the free surface, while downwellings are associated with weak surface-parallel stretching/compression. The growth and decay of the saddle intensity during upwelling events is clearly illustrated by Lagrangian autocorrelations

Finally, the clustering of the floating particles due to surface divergence is examined. The RDF and the Voronoi tessellation method indicate moderate clustering, consistent with the weak compressibility we observe. The clusters exhibit characteristic spatial and temporal scales greater than those of the divergence, suggesting the former is directly

affected by the large-scale motions. Taken together, the results of this study indicate that, in free-surface turbulence, the energetic scales leave a clearer imprint on the small-scale quantities compared with what is usually observed in 3-D turbulence.

We note that the surface contamination in the experiment could potentially affect the surface dynamics, including the surface-parallel fluctuation and surface divergence. However, this applies to other free-surface flows even when great care is taken in cleaning the surface. Our results are robust in that they do not change significantly with the time after the surface skimming. Still, it will be interesting to quantify differences in behaviour with respect to situations in which the surface is completely devoid of surfactants. Such a study poses evident challenges for large-scale set-ups such as the present one, and is beyond the scope of this work. Additionally, novel experiments are needed to determine the nature and the extent of surfactant-driven effects. Indeed, assessing the degree of contamination sufficient to alter the flow is also an unmet challenge. Recent measurements by Erinin *et al.* (2023), highlighted by Lohse (2023), indicated that the effect of surface contamination on plunging waves is controlled by the surface tension gradient rather than by the bulk value of surface tension in the undisturbed fluid. This might apply also to free-surface motion driven by bulk turbulence; this would explain the evidence of surface contamination, even though the measured bulk value of surface tension agrees with that of contaminant-free water. Verifying this picture warrants future investigations.

This work probes several fundamental aspects of free-surface flows, including the free-surface dissipation rate, the statistics and topology of velocity gradient, the Kolmogorov scaling in the inertial range and the effect of divergence on surface properties. The results may further shed light on other associated physical processes. In particular, the enhanced intermittency of the velocity gradient is found to be associated with the nonlinear self-amplification (Qi *et al.* 2025); the balance of vortex stretching and compression might explain the direction of energy cascade (Pan & Banerjee 1995; Lovecchio *et al.* 2015; Ruth & Coletti 2024); and the new scaling in the second-order structure function might account for the distinct dispersion behaviour of floating particles (Eckhardt & Schumacher 2001; Li *et al.* 2024). Several questions that are outside the scope of this work may be better understood leveraging the present findings, such as the exchange of mass and energy between the surface and the bulk, the inter-scale energy flux and the role of surface deformation in the dynamics of free-surface flow. Dedicated experiments that acquire data on the surface deformation, surface flow and flow in the bulk are required to tackle such problems.

Funding. Funding from the Swiss National Science Foundation (project no. 200021-207318) is gratefully acknowledged.

Declaration of interests. The authors report no conflict of interest.

Data availability statement. All the data supporting this work are available from the corresponding author upon reasonable request.

References

Babiker, O.M., Bjerkebæk, I., Xuan, A., Shen, L. & Ellingsen, S.Å. 2023 Vortex imprints on a free surface proxy for surface divergence. *J. Fluid Mech.* **964**, R2.

Balachandar, S. & Eaton, J.K. 2010 Turbulent dispersed multiphase flow. *Annu. Rev. Fluid Mech.* **42** (1), 111–133.

Banerjee, S. 1994 Upwellings, downdrafts, and whirlpools: dominant structures in free surface turbulence. *Appl. Mech. Rev.* **47** (6S), S166–S172.

Banerjee, S., Scott, D. & Rhodes, E. 1968 Mass transfer to falling wavy liquid films in turbulent flow. *Ind. Engng Chem. Fundam.* **7** (1), 22–27.

BEC, J., BIFERALE, L., CENCINI, M., LANOTTE, A. & TOSCHI, F. 2010 Intermittency in the velocity distribution of heavy particles in turbulence. *J. Fluid Mech.* **646**, 527–536.
BEC, J., GUSTAVSSON, K. & MEHLIG, B. 2024 Statistical models for the dynamics of heavy particles in turbulence. *Annu. Rev. Fluid Mech.* **56** (1), 189–213.
BECHLARS, P. & SANDBERG, R. 2017 Variation of enstrophy production and strain rotation relation in a turbulent boundary layer. *J. Fluid Mech.* **812**, 321–348.
BERK, T. & COLETTI, F. 2021 Dynamics of small heavy particles in homogeneous turbulence: a Lagrangian experimental study. *J. Fluid Mech.* **917**, A47.
BERK, T. & COLETTI, F. 2023 Dynamics and scaling of particle streaks in high-Reynolds-number turbulent boundary layers. *J. Fluid Mech.* **975**, A47.
BETCHOV, R. 1956 An inequality concerning the production of vorticity in isotropic turbulence. *J. Fluid Mech.* **1** (5), 497–504.
BEWLEY, G.P., SAW, E.-W. & BODENSCHATZ, E. 2013 Observation of the sling effect. *New J. Phys.* **15** (8), 083051.
BOFFETTA, G., DAVOUDI, J., & LILLO, F.D. 2006 Multifractal clustering of passive tracers on a surface flow. *Europhys. Lett.* **74** (1), 62–68.
BOFFETTA, G., DE LILLO, F., & A., GAMBA 2004 Large scale inhomogeneity of inertial particles in turbulent flows. *Phys. Fluids* **16** (4), L20–L23.
BRANDT, L. & COLETTI, F. 2022 Particle-laden turbulence: progress and perspectives. *Annu. Rev. Fluid Mech.* **54** (1), 159–189.
BROCCHINI, M. & PEREGRINE, D. 2001 The dynamics of strong turbulence at free surfaces. part 1. description. *J. Fluid Mech.* **449**, 225–254.
BRUMLEY, B.H. & JIRKA, G.H. 1987 Near-surface turbulence in a grid-stirred tank. *J. Fluid Mech.* **183**, 235–263.
BUXTON, O. & GANAPATHISUBRAMANI, B. 2010 Amplification of enstrophy in the far field of an axisymmetric turbulent jet. *J. Fluid Mech.* **651**, 483–502.
CALMET, I. & MAGNAUDET, J. 2003 Statistical structure of high-reynolds-number turbulence close to the free surface an open-channel flow. *J. Fluid Mech.* **474**, 355–378.
CARDESA, J., MISTRY, D., GAN, L. & DAWSON, J. 2013 Invariants of the reduced velocity gradient tensor in turbulent flows. *J. Fluid Mech.* **716**, 597–615.
CARTER, D., PETERSEN, A., AMILI, O. & COLETTI, F. 2016 Generating and controlling homogeneous air turbulence using random jet arrays. *Exp. Fluids* **57** (12), 1–15.
CARTER, D.W. & COLETTI, F. 2018 Small-scale structure and energy transfer in homogeneous turbulence. *J. Fluid Mech.* **854**, 505–543.
CHICKADEL, C., TALKE, S.A., HORNER-DEVINE, A.R. & JESSUP, A.T. 2011 Infrared-based measurements of velocity, turbulent kinetic energy, and dissipation at the water surface in a tidal river. *IEEE Geosci. Remote Sens. Lett.* **8** (5), 849–853.
CRESSMAN, J.R., DAVOUDI, J., GOLDBURG, W.I. & SCHUMACHER, J. 2004 Eulerian and Lagrangian studies in surface flow turbulence. *New J. Phys.* **6** (1), 53–53.
DAVIDSON, P. 2015 *Turbulence: an Introduction for Scientists and Engineers*. Oxford University Press.
DEIKE, L. 2022 Mass transfer at the ocean–atmosphere interface: the role of wave breaking, droplets, and bubbles. *Annu. Rev. Fluid Mech.* **54** (1), 191–224.
DONG, S., LOZANO-DURÁN, A., SEKIMOTO, A. & JIMÉNEZ, J. 2017 Coherent structures in statistically stationary homogeneous shear turbulence. *J. Fluid Mech.* **816**, 167–208.
DURHAM, W.M., CLIMENT, E., BARRY, M., DE LILLO, F., BOFFETTA, G., CENCINI, M., & STOCKER, R. 2013 Turbulence drives microscale patches of motile phytoplankton. *Nat. Commun.* **4** (1), 2148.
ECKHARDT, B. & SCHUMACHER, J. 2001 Turbulence and passive scalar transport in a free-slip surface. *Phys. Rev. E* **64** (1), 016314.
VAN EMMERIK, T., SCHWARZ, A. 2020 Plastic debris in rivers. *WIREs Water* **7** (1), e1398.
ERININ, M., LIU, C., LIU, X., MOSTERT, W., DEIKE, L. & DUNCAN, J. 2023 The effects of surfactants on plunging breakers. *J. Fluid Mech.* **972**, R5.
ESTEBAN, L., SHRIMPTON, J. & GANAPATHISUBRAMANI, B. 2019 Laboratory experiments on the temporal decay of homogeneous anisotropic turbulence. *J. Fluid Mech.* **862**, 99–127.
FERENC, J.-S. & NÉDA, Z. 2007 On the size distribution of poisson voronoi cells. *Physica A: Stat. Mech. Applics.* **385** (2), 518–526.
GEORGE, W.K. & HUSSEIN, H.J. 1991 Locally axisymmetric turbulence. *J. Fluid Mech.* **233**, 1–23.
GOLDBURG, W., CRESSMAN, J., VÖRÖS, Z., ECKHARDT, B. & SCHUMACHER, J. 2001 Turbulence in a free surface. *Phys. Rev. E* **63** (6), 065303.

GUO, X. & SHEN, L. 2010 Interaction of a deformable free surface th statistically steady homogeneous turbulence. *J. Fluid Mech.* **658**, 33–62.
HERLINA, & JIRKA, G. 2008 Experiments on gas transfer at the air–water interface induced by oscillating grid turbulence. *J. Fluid Mech.* **594**, 183–208.
HERLINA, H. & WISSINK, J. 2014 Direct numerical simulation of turbulent scalar transport across a flat surface. *J. Fluid Mech.* **744**, 217–249.
HERLINA, H. & WISSINK, J. 2019 Simulation of air–water interfacial mass transfer driven by high-intensity isotropic turbulence. *J. Fluid Mech.* **860**, 419–440.
HUNT, J. & GRAHAM, J. 1978 Free-stream turbulence near plane boundaries. *J. Fluid Mech.* **84** (2), 209–235.
JÄHNE, B. & HAUSSECKER, H. 1998 Air-water gas exchange. *Annu. Rev. Fluid Mech.* **30** (1), 443–468.
JOHNSON, P.L. & WILCZEK, M. 2024 Multiscale velocity gradients in turbulence. *Annu. Rev. Fluid Mech.* **56** (1), 463–490.
KOLMOGOROV, A.N. 1941 The local structure of turbulence in incompressible viscous fluid for very large reynolds numbers. *C. R. Acad. Sci. URSS* **30**, 301–305.
KOMORI, S., MURAKAMI, Y. & UEDA, H. 1989 Detection of coherent structures associated with bursting events in an open-channel flow by a two-point measuring technique using two laser-doppler velocimeters. *Phys. Fluids A: Fluid Dyn.* **1** (2), 339–348.
KUMAR, S., GUPTA, R. & BANERJEE, S. 1998 An experimental investigation of the characteristics of free-surface turbulence in channel flow. *Phys. Fluids* **10** (2), 437–456.
LAMONT, J. C. & SCOTT, D. 1970 An eddy cell model of mass transfer into the surface of a turbulent liquid. *AIChE J.* **16** (4), 513–519.
LARKIN, J., BANDI, M., PUMIR, A. & GOLDBURG, W. I. 2009 Power-law distributions of particle concentration in free-surface flows. *Phys. Rev. E—Stat. Nonlinear, and Soft Matter Phys.* **80** (6), 066301.
LI, Y., WANG, Y., QI, Y. & COLETTI, F. 2024 Relative dispersion in free-surface turbulence. *J. Fluid Mech.* **993**, R2.
LINDEMANN, C., VISSER, A. & MARIANI, P. 2017 Dynamics of phytoplankton blooms in turbulent vortex cells. *J. R. Soc. Interface* **14** (136), 20170453.
LOHSE, D. 2023 Surfactants on troubled waters. *J. Fluid Mech.* **976**, F1.
LOVECCHIO, S., MARCHIOLI, C. & SOLDATI, A. 2013 Time persistence of floating-particle clusters in free-surface turbulence. *Phys. Rev. E—Stat. Nonlinear, and Soft Matter Phys.* **88** (3), 033003.
LOVECCHIO, S., ZONTA, F. & SOLDATI, A. 2015 Upscale energy transfer and flow topology in free-surface turbulence. *Phys. Rev. E* **91** (3), 033010.
LOZANO-DURÁN, A., FLORES, O. & JIMÉNEZ, J. 2012 The three-dimensional structure of momentum transfer in turbulent channels. *J. Fluid Mech.* **694**, 100–130.
MAGNAUDET, J. 2003 High-Reynolds-number turbulence in a shear-free boundary layer: revisiting the Hunt Graham theory. *J. Fluid Mech.* **484**, 167–196.
MAXEY, M.R. 1987 The gravitational settling of aerosol particles in homogeneous turbulence and random flow fields. *J. Fluid Mech.* **174**, 441–465.
MCKENNA, S. & MCGILLIS, W. 2004 The role of free-surface turbulence and surfactants in air–water gas transfer. *Intl J. Heat Mass Transfer* **47** (3), 539–553.
MENEVEAU, C. 2011 Lagrangian dynamics and models of the velocity gradient tensor in turbulent flows. *Annu. Rev. Fluid Mech.* **43** (1), 219–245.
MOISY, F. & JIMÉNEZ, J. 2004 Geometry and clustering of intense structures in isotropic turbulence. *J. Fluid Mech.* **513**, 111–133.
MONCHAUX, R., BOURGOIN, M. & CARTELLIER, A. 2010 Preferential concentration of heavy particles: a voronoï analysis. *Phys. Fluids* **22** (10), 103304.
MORDANT, N., CRAWFORD, A.M. & BODENSCHATZ, E. 2004 Experimental Lagrangian acceleration probability density function measurement. *Physica D: Nonlinear Phenom.* **193** (1-4), 245–251.
MOUNTFORD, A.S. & MORALES MAQUEDA, M. 2019 Eulerian modeling of the three-dimensional distribution of seven popular microplastic types in the global ocean. *J. Geophys. Res.: Oceans* **124** (12), 8558–8573.
MULLIN, J.A. & DAHM, W.J. 2006 Dual-plane stereo particle image velocimetry measurements of velocity gradient tensor fields in turbulent shear flow. ii. experimental results. *Phys. Fluids* **18** (3), 035102.
NAGAOSA, R. 1999 Direct numerical simulation of vortex structures and turbulent scalar transfer across a free surface a fully developed turbulence. *Phys. Fluids* **11** (6), 1581–1595.
NIKORA, V., NOKES, R., VEALE, W., DAVIDSON, M. & JIRKA, G. 2007 Large-scale turbulent structure of uniform shallow free-surface flows. *Environ. Fluid Mech.* **7** (2), 159–172.
PAN, Y. & BANERJEE, S. 1995 A numerical study of free-surface turbulence in channel flow. *Phys. Fluids* **7** (7), 1649–1664.

PEROT, B. & MOIN, P. 1995 Shear-free turbulent boundary layers. part 1. physical insights into near-wall turbulence. *J. Fluid Mech.* **295**,199–227.
PETERSEN, A. J., BAKER, L. & COLETTI, F. 2019 Experimental study of inertial particles clustering and settling in homogeneous turbulence. *J. Fluid Mech.* **864**, 925–970.
PUMIR, A., BODENSCHATZ, E. & XU, H. 2013 Tetrahedron deformation and alignment of perceived vorticity and strain in a turbulent flow. *Phys. Fluids* **25** (3), 035101.
QI, Y., TAN, S., CORBITT, N., URBANIK, C., SALIBINDLA, A.K. & NI, R. 2022 Fragmentation in turbulence by small eddies. *Nat. Commun.* **13** (1), 469.
QI, Y., XU, Z. & COLETTI, F. 2025 Restricted Euler dynamics in free-surface turbulence. *J. Fluid Mech.* **1002**, A38.
RICHARDSON, L.F. 1926 Atmospheric diffusion shown on a distance-neighbour graph. *Proc. R. Soc. Lond. A.* **110** (756), 709–737.Containing Papers of a Mathematical and Physical Character.
RUTH, D.J. & COLETTI, F. 2024 Structure and energy transfer in homogeneous turbulence below a free surface. *J. Fluid Mech.* **1001**, A46.
SALMON, S., HENRI, R., BAKER, L.J., KOZAREK, J.L. & COLETTI, F. 2023 Effect of shape and size on the transport of floating particles on the free surface a natural stream. *Water Resour. Res.* **59** (10), e2023WR035716.
SCHUMACHER, J. & ECKHARDT, B. 2002 Clustering dynamics of Lagrangian tracers in free-surface flows. *Phys. Rev. E* **66** (1), 017303.
SHEN, L., ZHANG, X., YUE, D.K. & TRIANTAFYLLOU, G.S. 1999 The surface layer for free-surface turbulent flows. *J. Fluid Mech.* **386**, 167–212.
SREENIVASAN, K. 1991 Fractals and multifractals in fluid turbulence. *Annu. Rev. Fluid Mech.* **23** (1), 539–604.
SREENIVASAN, K.R. 1995 On the universality of the Kolmogorov constant. *Phys. Fluids* **7** (11), 2778–2784.
SREENIVASAN, K.R. & ANTONIA, R.A. 1997 The phenomenology of small-scale turbulence. *Annu. Rev. Fluid Mech.* **29** (1), 435–472.
TAMBURRINO, A. & GULLIVER, J.S. 2007 Free-surface visualization of streamwise vortices in a channel flow. *Water Resour. Res.* **43** (11), W11410.
TEIXEIRA, M. & BELCHER, S. 2000 Dissipation of shear-free turbulence near boundaries. *J. Fluid Mech.* **422**, 167–191.
THOMAS, N. & HANCOCK, P. 1977 Grid turbulence near a moving wall. *J. Fluid Mech.* **82** (3), 481–496.
TSAI, W.-T. & YUE, D.K. 1995 Effects of soluble and insoluble surfactant on laminar interactions of vortical flows with a free surface. *J. Fluid Mech.* **289**, 315–349.
TURNEY, D.E. & BANERJEE, S. 2013 Air–water gas transfer and near-surface motions. *J. Fluid Mech.* **733**, 588–624.
UZKAN, T. & REYNOLDS, W. 1967 A shear-free turbulent boundary layer. *J. Fluid Mech.* **28** (4), 803–821.
VARIANO, E.A. & COWEN, E.A. 2008 A random-jet-stirred turbulence tank. *J. Fluid Mech.* **604**, 1–32.
VARIANO, E.A. & COWEN, E.A. 2013 Turbulent transport of a high-Schmidt-number scalar near an air–water interface. *J. Fluid Mech.* **731**, 259–287.
VERON, F. 2015 Ocean spray. *Annu. Rev. Fluid Mech.* **47** (1), 507–538.
WALKER, D., LEIGHTON, R. & GARZA-RIOS, L.O. 1996 Shear-free turbulence near a flat free surface. *J. Fluid Mech.* **320**, 19–51.
WISSINK, J.G., HERLINA, H., AKAR, Y. & UHLMANN, M. 2017 Effect of surface contamination on interfacial mass transfer rate. *J. Fluid Mech.* **830**, 5–34.
YEUNG, P., DONZIS, D. & SREENIVASAN, K. 2012 Dissipation, enstrophy and pressure statistics in turbulence simulations at high reynolds numbers. *J. Fluid Mech.* **700**, 5–15.
YEUNG, P., ZHAI, X. & SREENIVASAN, K.R. 2015 Extreme events in computational turbulence. *Proc. Natl Acad. Sci. USA* **112** (41), 12633–12638.
ZHANG, H. 2017 Transport of microplastics in coastal seas. *Estuar. Coast. Shelf Sci.* **199**, 74–86.